Atmos. Chem. Phys., 26, 16545–16570, 2026
https://doi.org/10.5194/acp-26-16545-2026
© Author(s) 2026. This work is distributed under
the Creative Commons Attribution 4.0 License.

Atmospheric Chemistry and Physics
Open Access
EGU

Saharan dust transport and boundary layer entrainment over western Europe: multi-instrument observations and convection-permitting model evaluation

Hengheng Zhang[1], Gholam Ali Hoshyaripour[1], Heike Vogel[1,i], Frank Wagner[2], Thomas Leisner[1], Jochen Förstner[2], Prabhakar Shrestha[2], and Harald Saathoff[1]

[1]Institute of Meteorology and Climate Research, Karlsruhe Institute of Technology, Eggenstein-Leopoldshafen, Karlsruhe, Germany
[2]Deutscher Wetterdienst (DWD), Frankfurter Str. 135, 63067 Offenbach am Main, Germany
[i]retired

Correspondence: Hengheng Zhang (zhang@riam.kyushu-u.ac.jp) and Harald Saathoff (harald.saathoff@kit.edu)

Received: 1 December 2025 – Discussion started: 3 February 2026
Revised: 20 October 2026 – Accepted: 27 October 2026 – Published: 20 November 2026

Abstract. Long-range Saharan dust transport affects radiation, clouds, and air quality, yet its vertical structure and entrainment into the boundary layer remain challenging to simulate. We investigate four contrasting dust events over southwestern Germany using ground-based lidar, sun-photometer and in situ aerosol measurements, satellite observations, backward trajectories, and ICON-ART simulations. The events represent diverse atmospheric conditions, including a six-day cloud-free episode, a cloudy episode involving dust–cloud interactions, and an intense outbreak with aerosol optical depth approaching 1.4. A depolarization-based lidar method separated dust backscatter from contributions by other aerosols, enabling a like-for-like evaluation of the dust represented by ICON-ART and providing a useful approach for evaluating dust models in mixed aerosol layers. ICON-ART reproduced the large-scale transport and arrival of the dust layers, with mean differences of approximately 20 min in arrival time and 50 m in layer height. Daily re-initialization of the global simulations improved correlations with observed near-surface particulate matter concentrations from 0.65–0.69 to 0.86–0.88 and better reproduced the timing and persistence of boundary-layer dust. The benefits of higher resolution (2 and 1 km) become more apparent when combined with model reinitialization. However, ICON-ART consistently overestimated particles of 0.5–2 µm and underestimated particles larger than 2 µm. These results demonstrate the complementary benefits of accurate meteorological initialization and convection-permitting resolution while identifying size-dependent emission, sedimentation, and deposition as priorities for model development. By distinguishing errors in dust transport from those arising from aerosol size representation, this study provides an observation-constrained framework for evaluating and improving convection-permitting dust forecasts.

1 Introduction

The Saharan desert is the largest source of aeolian dust in the world, with annual production rates of about 4–7×10^8 t yr^{-1}, which is almost half of all aeolian dust inputs to the oceans (Middleton and Goudie, 2001). Saharan dust is mainly produced by natural processes such as wind storms and does not appear to be heavily impacted by human activities (Kandler et al., 2007). Saharan dust has been found to be transported in the free troposphere over long distances reaching e.g.the Amazon basin, middle and north America, Europe (Guerzoni and Chester, 1996), even Japan (Tanaka et al., 2005), and other regions. The Saharan dust impacts ecosystems and human life in the following ways. Firstly, dust impacts ecosystems in various regions like the Atlantic

Ocean, the Amazon basin, the southeastern United States, or the Caribbean by providing nutrients such as phosphorus or iron, and in some cases promoting soil development (Molinaroli et al., 1993). Secondly, Saharan dust has also impact on power supply by changing photovoltaic output. When it comes to Saharan dust outbreaks, the photovoltaic output is reduced not only through a significant increase in aerosol optical thickness, but also through dust deposition on the photovoltaic modules on subsequent days (Conceição et al., 2018; Rieger et al., 2017a). Thirdly, Saharan dust particles can also act as cloud condensation nuclei (CCN) or ice-nucleating particles (INP), influencing cloud formation and thereby altering radiative forcing through aerosol indirect effects (Seifert et al., 2023). Finally, Saharan dust outbreaks have impact on short-range weather forecast errors as current weather prediction models still struggle to reproduce cloudiness and radiative effects during dust events, largely because of missing or simplified representations of aerosol–cloud interactions, especially the indirect effects of dust (Hermes et al., 2024).

Changes in circulation patterns associated with climate change have led to an increase in frequency and intensity of Saharan dust events in the Carpathian Basin (Varga, 2020). The annual number of dust events was 4.2 on average between 1979 and 2010, while in the period of 2011–2018, it has increased to 10.3. And an average of about 33 000 t of atmospheric dust was transported to Central Europe each year from 2002–2017 (Rostási et al., 2022). The increased frequency and amount of Sahran dust loading have caused larger uncertainties in global radiative forcing (Saidou Chaibou et al., 2020; Diop et al., 2020; Mallet et al., 2009).

The predictions of dust layer regarding dust arrival time, dust height and structure, as well as dust impact on clouds, precipitation, and convective systems is becoming more important. In past decades, different transport models were developed to simulate the distribution and evolution of aerosol over the globe. For example, the general circulation model the ECHAM-HAMMOZ (Pozzoli et al., 2008a, b), the ECHAM/MESSy Atmospheric Chemistry (EMAC) (Roeckner et al., 2006; Jöckel et al., 2006, 2010), the Whole Atmosphere Community Climate Model (WACCM) (Kunz et al., 2011; Smith et al., 2011), the Weather Research and Forecasting (WRF) model coupled with Chemistry (WRF/Chem) (Chapman et al., 2009), the CONsortium for small-scale MOdeling (COSMO) and its extension on Aerosol and Reactive Trace gases (ART) (Vogel et al., 2014), and its successor the ICOsahedral Nonhydrostatic (ICON) and its extension on Aerosol and Reactive Trace gases (ART) (Hoshyaripour et al., 2026; Rieger et al., 2015; Weimer et al., 2017). A multi-model forecast comparison is now also available by the Sand and Dust Storm Warning Advisory and Assessment System (Benincasa, 2023), a program of the World Meteorological Organization (WMO). The Dust-DN (Dust Doctoral Network) project, an EU-funded initiative under the Horizon Europe program, seeks to advance the scientific understanding of mineral dust processes and improve the predictive capabilities of online coupled chemistry transport models (https://dust-dn.cyi.ac.cy/, last access: 26 December 2024).

Different online coupled chemistry transport models need to be evaluated against a range of measurement methods, including both remote sensing and in-situ observations. This comparison is essential for validating model performance, assessing the validity of parameterizations used in the models, and improving our understanding of aerosol properties and processes during dust events (Zhang et al., 2022; Hoshyaripour et al., 2019). For example, aerosol lidar is a useful tool to validate Saharan dust model simulations as it can provide high-resolution vertical profiles of Saharan air layers (SALs) (Chouza et al., 2016; Zhang et al., 2022). Ground-based lidar networks including the European Aerosol Research Lidar Network (EARLINET) (Mona et al., 2014), the Micro-Pulse Lidar Network (MPLNET) (Misra et al., 2012), and the Asian Dust and Aerosol Lidar Observation Network (AD-Net) (Sugimoto et al., 2016) have conducted long-term dust observation in last decades to investigate dust transport and optical proprieties. Also the sun photometers deployed by the Aerosol Robotic Network (AERONET) (Kim et al., 2011) provides rich information on column integrated dust optical parameters (e.g. Aerosol optical depth (AOD), Ångström Exponent (AE), single scattering albedo (SSA)). Finally, satellite data can be also used to study Saharan dust proprieties and validate online coupled chemistry transport model. For example, the MODIS instrument aboard the Terra & Aqua satellites can provide column integrated aerosol optical properties (Merdji et al., 2023; Barnaba and Gobbi, 2004) and the Cloud-Aerosol Lidar with Orthogonal Polarization (CALIOP) aboard of the CALIPSO satellite can provide vertical profiles of aerosol information (Hoshyaripour et al., 2019; Liu et al., 2008). The valuable satellite data provided by these active or passive remote sensing sensors aboard different satellites help to understand the dust proprieties over the globe (Song et al., 2022; Wu et al., 2020).

Central Europe, provides an excellent location for investigating SALs. Firstly, this region is frequently affected by long-range transported Saharan dust events, especially during spring and summer seasons (Ansmann et al., 2003; Gasteiger et al., 2011). Second, the typical transport time for dust particles – ranging from 2 to 5 d – makes it ideal for examining long-range dust transport and its interactions with local atmospheric conditions (Ansmann et al., 2003). Additionally, the region's diverse meteorological patterns, including extreme weather events such as storms and prolonged dry periods, play a significant role in dust movement and deposition, offering a wide range of scenarios for analysis (Kunz et al., 2022b). These factors make southwest Germany a key site for validating global transport models, with insights gained here being broadly applicable to other regions with similar characteristics.

Zhang et al. (2022) investigated the properties and transport of Saharan dust during the period from 7 to 9 April 2018,

through a synergistic approach combining modeling and observational data. They demonstrated that a novel method for retrieving the lidar ratio from scanning aerosol lidar measurements could be effectively applied to the Saharan Air Layer (SAL), yielding optical parameters (e.g., lidar ratio and particle depolarization ratio) consistent with values reported in the literature. Their study also showed that the modeled backscatter coefficients agreed well with lidar observations when non-spherical particles were assumed, with a slope of 0.9 ± 0.1 ($R^2 = 0.68$). In contrast, assuming spherical particles led to a significant overestimation, with a slope of 2.3 ± 0.3 ($R^2 = 0.74$). In the present study, we utilize a more comprehensive dataset to investigate the evolution and optical properties of dust in southwest Germany, extending the analysis to a broader set of dust events and characteristics. A scanning aerosol lidar system, a sun photometer, different ground-level in-situ aerosol characterisation instruments (e.g. Optical Particle counter (OPC)), the CALIPSO, the MODIS, and a online coupled aerosol and chemistry transport model, ICON-ART model (Hoshyaripour et al., 2026), were employed in 4 Saharan dust cases to investigate these dust events employing different retrieval methods. Three of these events are discussed in detail in this study. Case 1 was previously examined by Zhang et al. (2022), but it is also included here in the statistical analysis. The objectives of this study are to (1) characterize the transport pathways, vertical structure, optical properties, and size distributions of Saharan dust using a unique combination of ground-based, in-situ, and satellite observations; (2) evaluate the ability of ICON-ART to reproduce these observed dust characteristics; and (3) investigate the influence of model resolution and meteorological initialization on the representation of long-range transported Saharan dust over Europe.

This paper is organised as follows. Section 2 describes the remote sensing and in situ methods as well as the model simulations. Details of the dust observations and dust properties are discussed in Sect. 3 including a comparison of the different remote sensing and in situ methods as well as how they compare to the model predictions. In the final section, we provide some conclusions.

2 Method

Four Saharan dust events were investigated combining remote sensing, ground-level in situ measurements, and ICON-ART model over western Europe. The four selected cases were chosen to sample a broad range of aerosol and cloud conditions. Case 1 was discussed detailedly by Zhang et al. (2022). Case 2 corresponds to the longest cloud-free Saharan dust episode, lasting approximately six days, and serves as a reference case for examining the temporal evolution and vertical structure of SALs under clear-sky conditions. Case 3 documents the interaction between Saharan dust and clouds, allowing an investigation of dust–cloud coupling processes and their influence on observed vertical structures. Case 4 represents the most intense dust outbreak, with aerosol optical depth (AOD) approaching 1.4, and is used to assess the vertical distribution and optical characteristics of extremely dense dust layers. Together, these cases provide a comprehensive framework for evaluating lidar observation strategies and for characterizing Saharan dust under diverse atmospheric conditions. A scanning aerosol lidar (Zhang et al., 2022) provided spatial-temporal distributions of SALs and optical proprieties of dust particles. Also, a sun photometer (Giles et al., 2019) provided wavelength-dependent aerosol optical depth (AOD), Angstrom exponent (AE), and under clear sky conditions the aerosol size distributions (ASD), and single scattering albedo (SSA). Besides, ground-level in situ aerosol characterisation instruments (e.g. OPC, APS, SMPS, and CPC) provided aerosol number concentration and mass concentration as well as aerosol size distribution. Finally, these observational data were compared with forecasts from ICON-ART (Hoshyaripour et al., 2026). The model is running in operational mode by Deutscher Wetterdienst (DWD) since March 2024. The main methods used to characterize the four different Saharan dust events are summarized in Table 1.

2.1 Remote sensing methods

Karlsruhe scanning aerosol lidar (KASCAL (LR111-ESS-D200, Raymetrics Inc.)) was deployed at the campus north of the Karlsruhe Institute of Technology (8.4298° E, 49.0953° N, 119 m above sea level) during the dust event of April 2018, February 2021, and March 2022. It was deployed in Rottenburg am Neckar (8.95452° E, 48.4892° N, 339 m above sea level) for dust events that occurred on June 2021 (Kunz et al., 2022b). The KASCAL lidar system is a mobile scanning system with an emission wavelength of 355 nm. The laser head, 200 mm telescope, and lidar signal detection units are mounted on a rotating platform. The overlap range of the lidar system is 255 m and the overlap correction for the KASCAL lidar has been done with horizontal measurements assuming horizontal homogeneous conditions. The KASCAL lidar operates automatically and continuously according to a predefined schedule using software developed by Raymetrics Inc.a software developed by Raymetrics Inc. (Avdikos, 2015). For the data analysis and calibration of the system, we followed the quality standards of the European Aerosol Research Lidar Network (EARLINET) (Freudenthaler, 2016; Zhang et al., 2022).

Tesche et al. (2009b) proposed a method to separate the total backscatter coefficient into a dust part and a non-dust part using the following equation:

$$\beta_{\lambda,\mathrm{d}} = \beta_{\lambda,\mathrm{p}} \frac{(\delta_{\lambda,\mathrm{p}} - \delta_{\lambda,\mathrm{nd}})(1 + \delta_{\lambda,\mathrm{d}})}{(\delta_{\lambda,\mathrm{d}} - \delta_{\lambda,\mathrm{nd}})(1 + \delta_{\lambda,\mathrm{p}})} \quad (1)$$

where $\beta_{\lambda,\mathrm{d}}$ is the pure dust backscatter coefficient, $\beta_{\lambda,\mathrm{p}}$ is the total particle backscatter coefficient, $\delta_{\lambda,\mathrm{p}}$ is the total particle

Table 1. List of available ground/satellite observations and model forecasts for the Saharan dust events (SPH[a]: Sun photometer; KIT-CN[b]: KIT campus north). Please note that the dust particles did not reach ground level during events 1 and 4 so that no in situ measurements could be conducted.

ID	Date	Observation site	lidar	OPC	APS	SPH[a]	ICON-ART
1	7–9 April 2018	KIT-CN[b], (8.4298° E, 49.0953° N)	X			X	X ($\Delta = 26$ km)
2	22–27 February 2021	KIT-CN, (8.4298° E, 49.0953° N)	X	X	X	X	X ($\Delta = 26$, 13, 2, 1 km)
3	19–20 June 2021	Rottenburg, (8.95452° E, 48.4892° N)	X	X	X	X	X ($\Delta = 26$ km)
4	16–22 March 2022	KIT-CN, (8.4298° E, 49.0953° N)	X			X	X ($\Delta = 26$ km)

depolarization ratio, $\delta_{\lambda,\mathrm{nd}}$ is the particle depolarization ratio of non-dust particles, $\delta_{\lambda,\mathrm{d}}$ is the particle depolarization ratio of the pure dust particle. In this equation, $\beta_{\lambda,\mathrm{p}}$ and $\delta_{\lambda,\mathrm{p}}$ can be retrieved from lidar measurement.

The sun photometer (CE-318, CIMEL, Holben et al. (1998)) which measures solar radiance at nine different wavelengths ranging from 339 to 1638 nm was also deployed in these four Saharan dust events. The sun photometer data enables calculation of AOD at specific wavelengths. Additionally, the data can be used to determine other important aerosol parameters such as (Single Scattering Albedo (SSA), Ångström Exponent (AE), (Aerosol Size Distribution(ASD, and complex refractive index (CRI) (Vermeulen et al., 2000; Sinyuk et al., 2020; Dubovik and King, 2000). SSA measures the ratio of scattering coefficient to extinction coefficient, which is inversely proportional to the aerosol absorption ability. AE describes the wavelength dependency of AOD, which is influenced by particle size. Smaller particles exhibit a stronger wavelength dependency, resulting in a higher AE value. Additionally, clear sky measurements from the sun photometer can be used to derive ASD (between 0.05–15 µm), complex refractive index (between 1.33–1.6 and $0.0005i$–$0.5i$), and other parameters (Dubovik and King, 2000; Müller et al., 2010). The sun photometer is part of the Aerosol Robotic Network (AERONET) and level 2.0 data was utilized in this study (Giles et al., 2019).

2.2 Ground-level in-situ instruments

The ground-level in-situ instruments were deployed in a mobile container for the field campaign at Rottenburg am Neckar and were installed in the laboratory of building 322 on campus north of the KIT near the village of Eggebstein-Leopoldshafen. Aerosol particle size distributions were measured using scanning mobility particle sizer (SMPS; DMA: TSI 3080, CPC 3022A, TSI Inc., 14–760 nm), aerodynamic particle sizer (APS; TSI 3321, TSI Inc, 0.5–20 µm), and optical particle counter (OPC; Fidas200, Palas, GmbH, 0.18–18 µm). Additionally, two condensation particle counters (CPC3776, 3025, TSI Inc.) were used for counting particle numbers (> 2.5 nm) with a time resolution of 1 s. These instruments operated with a flow rate of 5 L min^{-1} and a time resolution of 1–5 min during Saharan dust events 2 and 3. Meteorological parameters were measured using a compact sensor (WS7000, Luff) (Jiang et al., 2025).

2.3 ICON-ART data and simulations

To predict the transport and distribution of dust during the four Saharan dust events, the ICON-ART model system was used. ICON-ART is an online-coupled chemistry transport modelling system that combines numerical weather prediction and climate modelling with the representation of aerosols and trace gases, including their life cycle and interactions with radiation and clouds (Hoshyaripour et al., 2019). The ICON model solves the fully compressible, non-hydrostatic three-dimensional Navier–Stokes equations on an icosahedral grid (Zängl et al., 2015), while the ART extension includes aerosol and trace gas processes (Hoshyaripour et al., 2026). In this study ICON-ART only simulates the mineral dust with radiation coupling. However, the indirect effect is not simulated in the results presented here. ICON-ART predicts mass and number mixing ratio of mineral dust for three modes which are assumed to be lognormally distributed with fixed standard deviation. The median diameter is a diagnostic variable with mass median diameters of 1.5, 6.7, and 14.2 µm, and geometric standard deviations of 1.7, 1.6, and 1.5, respectively. Dust emissions are parameterized following Vogel et al. (2006) and Rieger et al. (2017b), accounting for soil properties, soil aggregation state, and soil-type heterogeneity. The model further considers major dust removal processes, including sedimentation as well as dry and wet deposition. The Aerosol Optical Depth (AOD) and backscatter coefficients are diagnosed at 550 and 532 nm respectively, assuming non-sphericity of the dust particles(Hoshyaripour et al., 2019).

The ICON-ART data used in this study originate from two different model configurations. For the baseline analysis of the four measurement campaigns, forecast data were obtained from the quasi-operational dust forecasting system of the Deutscher Wetterdienst (DWD). The forecasting system consists of a global domain coupled to a regional nest over North Africa and Europe, with horizontal resolutions of 40 and 20 km, respectively. The model employs 65 vertical layers, with layer thickness increasing from near surface layer height of 10 m to several kilometers in the upper atmosphere. In the altitude range between 2 and 6 km, where long-range

transported dust layers are frequently observed, the vertical resolution is approximately 200–400 m.

For the February 2021 case study, dedicated high-resolution ICON-ART simulations were performed specifically for this study using the regional limited-area mode (LAM) configuration with an additional nested domain, employing horizontal resolutions of 2 and 1 km, respectively. The lateral boundary conditions for the LAM simulations were provided by a 13 km European domain embedded within a 26 km global domain. This high-resolution setup was designed to better resolve mesoscale processes and to investigate the causes of discrepancies between simulations and observations in greater detail. We used the quasi-operational global ICON experiments with mineral dust at 40 km resolution available from the DWD servers to generate the initialized analysis at current operational global (ICON) and nested grid (ICON-NA2: North Africa North Atlantic) at 26 and 13 km, respectively. Here, it has to be noted that the analysis is only available for the meteorological variables, while no analysis exists for the dust tracers. So, an error source based on the model parameterization of dust emission, deposition remains. We acknowledge this important short-coming for modelled dust in the study. Nevertheless, the model provides valuable information about the spatial transport of dust at high resolution from the Saharan desert to Europe. Using the initialized analysis on 12:00 UTC on 21 February 2021, we make a 5 d forecast run (EXP-5d). For limited area mode (LAM) runs at higher resolution over Germany (ICON-D2: 2 km) with nest over Alpine region (ICON-A1: 1 km), we remap the initialized analysis to LAM grids and use the hourly boundary conditions from EU-NA2 nest for the 5 d forecast. In addition, we also conducted a 24 h forecast run with the Global runs using re-initialization at 12:00 UTC for the same 5 d period (RI-EXP-1d). The re-initialization is again based on the archived global ICON experiments at 40 km resolution. For the LAM runs, we use the initial conditions on 21 February 2021 and make a 5 d forecast run using the updated lateral boundary condition files from re-initialized global runs with nest.

3 Results

To investigate the dominant physical processes controlling Saharan dust transport over Western Europe, four representative meteorological scenarios are analyzed combining remote sensing, in situ measurements, and ICON-ART model calculations. The transport of the four SALs were first investigated by the HYbrid Single-Particle Lagrangian Integrated Trajectory (HYSPLIT) model. The hourly seven-day backward trajectories were calculated during Saharan dust periods for altitudes from 500 to 7500 m with an interval of 1000 m based on the HYSPLIT model. The frequency of these trajectories at two altitudes levels (Low altitude: 500 m and High altitude: 1500–7500 m) is shown in Fig. 1. The reasons for classifying these trajectories into two groups is that the trajectories at an altitude of 500 m are related to the transport of aerosol within the boundary layer while the high-altitude (1500–7500 m) ones are related to the long-distance transport in the free troposphere. The frequency map of high altitude trajectories shown at the bottom of Fig. 1 indicates that most of the trajectories originated from north Africa (Sahara Desert) as expected. However, the places of origin are different at low-altitude for these 4 Saharan dust cases. In case 1, most of the air parcel trajectories originated over the Atlantic Ocean, indicating that sea salt aerosols were likely transported over a long distance from the ocean to the study area by prevailing winds. During cases 2 and 3, most of the low-altitude trajectories also originated from north Africa (Sahara Desert), which is the reason why the Saharan dust particles could be measured by ground in situ instruments during this case. During case 4, The low-altitude trajectories originate over continental Europe or the Mediterranean region, which is related to the transport of local aerosol.

3.1 Evolution of Saharan dust events under different meteorological conditions

3.1.1 Long-lasting cloud-free dust event (case 2)

Dust case 2 was characterized by a persistent Saharan dust plume that reached Karlsruhe on 22 February 2021, progressively descended toward the surface, and remained over the region for nearly five days. Among the three dust events observed at KIT Campus North in February 2021, this event occurred predominantly under cloud-free conditions and was therefore particularly suitable for evaluating the transport and vertical evolution of Saharan dust. The MODIS daily mean AOD fields in Fig. S2 in the Supplement show the large-scale transport of the dust plume from North Africa toward Central Europe. At Karlsruhe, KASCAL observations indicate that the dust layer arrived at approximately 04:00 UTC on 22 February (T1), initially with maximum backscatter near 2.0 km altitude, and subsequently descended to the surface by approximately 10:00 UTC on 23 February (T2). Surface aerosol loading then increased markedly between 24 and 26 February, as indicated by the Fidas 200 mass size distributions and PM concentrations, whereas the corresponding increase in total particle number concentration was less pronounced because particle number was dominated by the smaller aerosol fraction. At approximately 12:00 UTC on 26 February (T5), both the lidar and surface measurements showed a rapid decrease in aerosol loading, coinciding with stronger winds and the advection of cleaner air masses.

ICON-ART reproduces the timing and broad vertical evolution of the event, but the comparison reveals larger discrepancies after the dust becomes increasingly mixed into the lower atmosphere. In the simulation, the plume reaches Karlsruhe at approximately 04:00 UTC on 22 February and persists for about five days, consistent with the observed du-

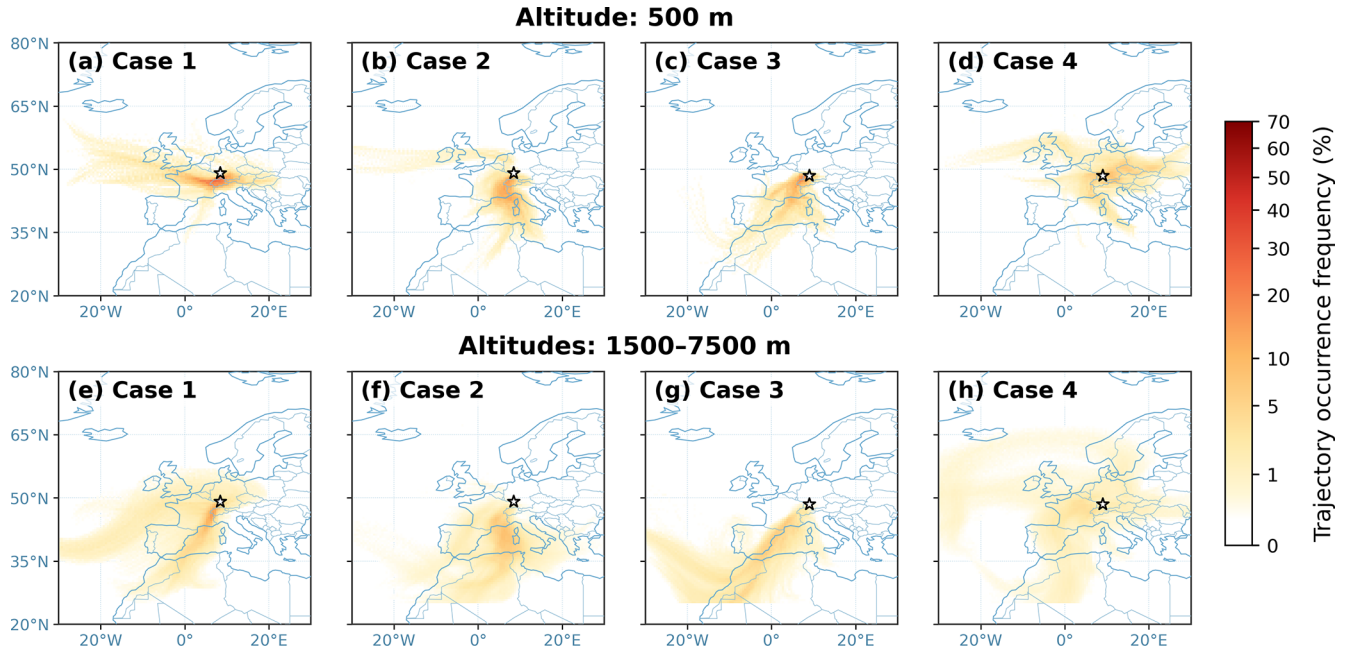


Figure 1. Frequency of trajectories at two altitude levels (500 and 1500–7500 m) during four Saharan dust case periods based on back trajectories calculated by the HYbrid Single-Particle Lagrangian Integrated Trajectory (HYSPLIT) model. (The case IDs are labeled in Table 1).

ration. During the early stage of the event, simulated dust backscatter extends from approximately 1 to 8 km. After 18:00 UTC on 24 February, the upper part of the simulated dust layer between approximately 3 and 8 km progressively weakens, while dust below 3 km becomes increasingly concentrated toward the surface.

At ground level, the simulated dust mass concentration follows the temporal variability of measured PM_{10} with a regression slope of 0.754 ± 0.041 and a correlation coefficient of 0.662 (Fig. 2g). The vertical evolution is likewise broadly reproduced, including the gradual descent of the dust layer, but the agreement deteriorates within the boundary layer after 24 February, where mineral dust becomes mixed with other aerosol components. The lower-atmospheric discrepancy is largely associated with aerosol composition rather than with a uniform bias in the simulated mineral-dust backscatter. After 18:00 UTC on 24 February, enhanced boundary-layer aerosol produces strong backscatter close to the surface and makes the elevated dust peak difficult to identify unambiguously from the lidar observations. This effect is particularly evident during period C2, when mineral dust and boundary-layer aerosol are mixed below approximately 2.0 km. Figure 3 quantifies the impact of this mixing by comparing ICON-ART backscatter coefficients with KASCAL retrievals between 20:00 UTC on 24 February and 12:00 UTC on 26 February 2021. When total aerosol backscatter is considered, the KASCAL values are larger than the ICON-ART dust backscatter by a factor of 1.94 ± 0.65. In contrast, after isolating the dust contribution in the lidar retrieval, the relationship with ICON-ART yields a regression slope of 0.974 ± 0.01, although the Pearson correlation coefficient remains moderate at 0.543. The near-unity slope therefore indicates that the systematic difference in backscatter magnitude is strongly reduced when only mineral dust is compared, whereas the remaining point-to-point variability reflects differences in the detailed temporal and vertical distribution. This comparison supports the interpretation that much of the enhanced total lidar backscatter in the lower atmosphere originates from non-dust aerosol that is not represented by the mineral-dust simulation. The sun-photometer and in situ size-distribution measurements independently confirm that the event was dominated by coarse particles while also revealing the progressive redistribution of dust from the elevated layer toward the surface. Figure 4 shows that the Ångström exponent (AE) remained below approximately 0.3 for most of the event, consistent with weak wavelength dependence associated with a dominant coarse-particle contribution. The AOD at 340 nm increased from 0.41 at 07:22 on 23 February to 0.66 at 15:57 on 24 February before decreasing to 0.42 at 16:00 UTC on 25 February. The wavelength dependence of the single-scattering albedo, including its lower value near 439 nm, is also consistent with stronger dust absorption at shorter wavelengths. Both the column-integrated volume size distributions retrieved from the sun photometer and the surface mass size distributions measured by the Fidas 200 show an enhanced contribution from particles larger than 1 µm. However, their temporal maxima occur on different days:

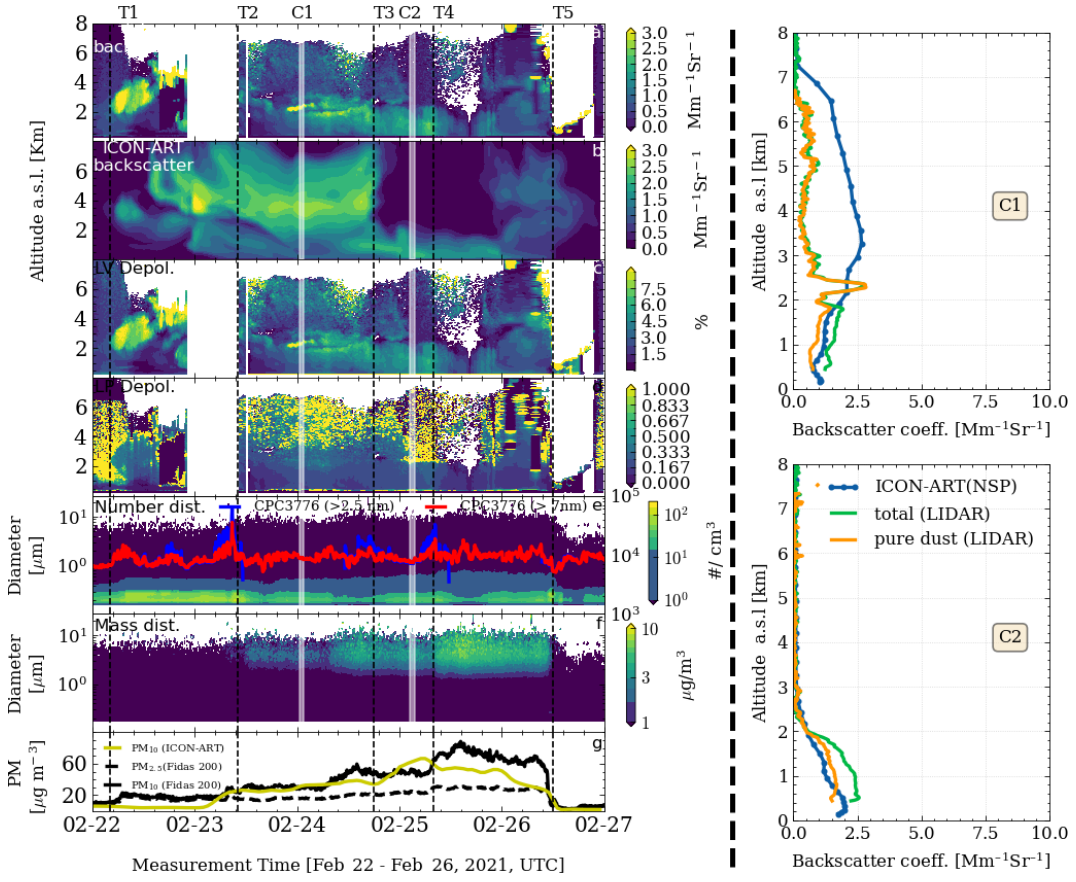


Figure 2. Time series of backscatter coefficients from KASCAL measurements **(a)**, predicted backscatter coefficients by ICON-ART **(b)**, Linear Volume Depolarization Ratio (LVDR) **(c)** Linear Particle Depolarization Ratio (LPDR) **(d)** from KASCAL measurements, particle number size distribution from Fidas 200 and particle number concentration from two CPCs **(e)**, particle mass size distribution from Fidas 200 **(f)** and particulate matter concentrations (PM_{10} and $PM_{2.5}$) from the Fidas 200 and the lowest model level (150 m) of the ICON-ART simulation **(g)** from 22 to 26 February 2021 for case 2. The profiles of backscatter coefficients measured by the lidar and predicted by ICON-ART model for case C1 (Averaged profiles from 00:30 to 01:30 for lidar measurement and profile at 01:00 UTC for ICON-ART prediction on 24 February 2021) and for a selected time C2 (Averaged profiles from 02:30 to 03:30 for lidar measurement and profile at 03:00 UTC for ICON-ART prediction on 25 February 2021) are shown on the right side of this figure. The vertical dashed lines in the contour plots indicate dust arrival (T1), dust touched to the ground (T2), an increase of PM concentration at ground level (T3 and T4) and a low-level cloud appeared (T5). C1 and C2 represent time periods used for a more detailed data analysis as shown in the right side of this figure.

the column-integrated aerosol volume concentration peaks on 24 February, whereas the surface aerosol mass concentration reaches its maximum on 25 February. This one-day offset is consistent with the lidar-observed descent of the dust layer. On 24 February, a substantial fraction of the dust remains aloft and therefore contributes strongly to the column-integrated sun-photometer retrieval but less to the surface measurements. By 25 February, more of the dust has descended into the boundary layer, increasing the aerosol mass concentration measured by the Fidas 200 even though the total column aerosol loading has already begun to decrease.

The comparison of observed and simulated AOD further shows that the ICON-ART bias changes sign during different stages of the event, indicating that a single systematic model error cannot explain the full five-day evolution. Figure S3 compares total and coarse-mode AOD measured by the sun photometer at 500 nm with ICON-ART AOD at 550 nm and separates the event into three periods. During periods A and C, the observed coarse-mode AOD exceeds the modeled AOD by a factor of 2.03 ± 1.34, whereas during period B the ICON-ART AOD is larger than the observed value by a factor of 1.98 ± 0.28. During period A, corresponding to the initial arrival and rapid increase of the dust plume, the model underestimation may reflect insufficient dust loading during emission and/or long-range transport. During period B, when dust remains over Central Europe under persistent dry conditions, the reversal toward model overestimation suggests that errors in vertical redistribution or removal processes may become more important. During period C, as the event decays and cleaner air reaches the region, the model again tends to

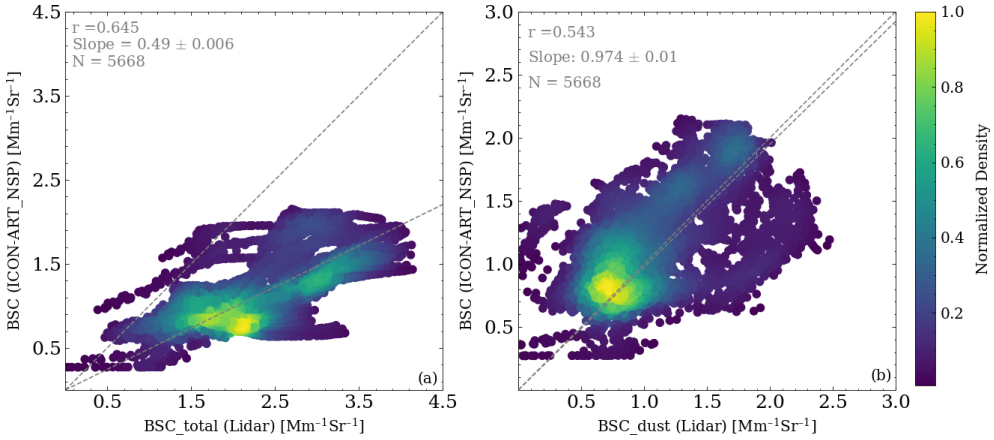


Figure 3. Correlation of backscatter coefficients predicted by ICON-ART and those retrieved from KASCAL for both total aerosol particles **(a)** and dust particles only **(b)** (from 20:00 UTC on 24 to 12:00 UTC to 26 February 2021 for case 2).

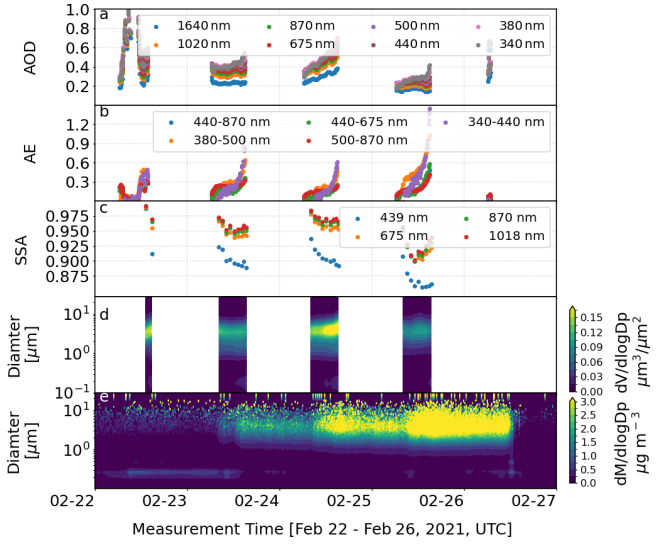


Figure 4. Time series of Aeosol Optical Depth (AOD) **(a)**, Ångström Exponent (AE) **(b)**, Single Scattering Albedo (SSA) **(c)** at different wavelengths, and column-averaged aerosol volume size distribution **(d)** measured and retrieved from sun photometer (AERONET, Karlsruhe station) as well as particle mass size distributions **(e)** measured by Fidas 200 from 22 to 26 February 2021 for case 2.

underestimate the observed aerosol loading. The change in both magnitude and sign of the AOD bias across the three periods therefore suggests that the model discrepancy evolves with the synoptic and transport stage of the event rather than arising from a single constant scaling error.

3.1.2 Dust-cloud interaction (case 3)

Saharan dust case 3 was characterized by a two-day dust event whose evolution was strongly modulated by clouds and precipitation during the Swabian MOSES campaign near Rottenburg, western Germany (Kunz et al., 2022b). The event occurred during IOP4 on 19–20 June 2021, and its large-scale transport toward southwestern Germany is illustrated by the MODIS daily mean AOD fields in Fig. S4. Because clouds substantially affected the Klett–Fernald retrieval, quantitative backscatter coefficients and LPDR from KASCAL are not used throughout the full event; instead, the temporal evolution is primarily characterized using the cross-polarized range-corrected signal and LVDR in Fig. 5. The first elevated dust layer arrived at approximately 11:00 UTC on 19 June (T1), with enhanced depolarization near 4 km, and subsequently descended toward approximately 2 km. A second dust layer reached the site at around 22:00 UTC and progressively extended into the lower atmosphere after 00:30 on 20 June (T2). This downward transport was accompanied by increasing surface aerosol concentrations until approximately 03:30 (T3). The surface evolution was interrupted by precipitation: drizzle around 03:00 UTC reduced aerosol concentrations, followed by renewed near-surface aerosol loading after approximately 11:30 (T4), and a further decrease associated with precipitation later on 20 June. Thus, unlike the predominantly cloud-free case 2, the observed aerosol evolution in case 3 reflects the combined effects of dust transport, vertical redistribution, and intermittent wet removal.

ICON-ART captures the arrival and broad vertical development of the dust plume, but shows substantial differences in layer height and surface concentration during this cloud-affected period. The model reproduces the arrival of the dust plume at approximately 11:00 UTC on 19 June and simulates elevated dust between about 4 and 5 km during the initial stage, followed by a deeper layer extending from near the surface to approximately 6 km after 23:30. Before cloud and precipitation strongly limit the lidar retrieval after 02:00 UTC on 20 June, the simulated dust-layer top is on average 900 ± 693 m higher than that derived from KAS-

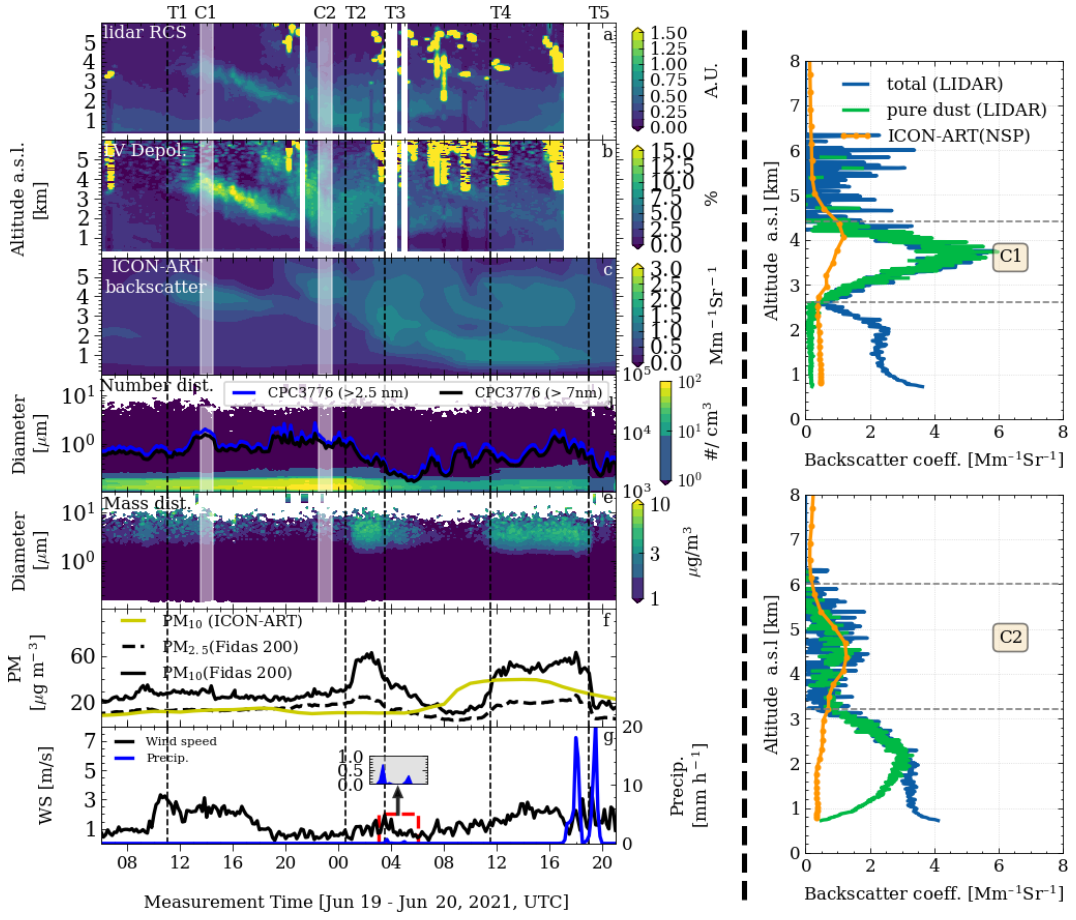


Figure 5. Time series of range corrected lidar signal for the cross-polarized channel **(a)**, and Linear Volume Depolarization Ratio (LVDR) from KASCAL measurements **(b)**, backscatter coefficients predicted by ICON-ART **(c)**, particle number size distributions from Fidas 200 and particle number concentration from two CPCs **(d)**, particle mass size distributions from Fidas 200 **(e)** and particulate matter concentrations (PM_{10}) from the Fidas 200 and the lowest model level (150 m) of the ICON-ART simulation **(f)**, and ground level meteorological parameters (e.g. wind, precipitation, WS700) **(g)** from 19 to 20 June 2021 for case 3. The profiles of backscatter coefficients measured by the lidar and predicted by the ICON-ART model for case C1 (averaged profiles from 13:30 to 14:30 for lidar measurements and profile at 14:00 UTC for ICON-ART prediction on 19 June 2021) and for case C2 (averaged profiles from 22:30 to 23:30 for lidar measurements and profile at 23:00 UTC for ICON-ART prediction on 19 June 2021) are shown on the right side of this figure. The vertical dashed lines in the contour plots indicate dust arrival (T1), dust touched to the ground (T2 and T4), and dust particle removal due to precipitation (T3 and T5). C1 and C2 represent time periods used for a more detailed data analysis as shown in the right side of this figure.

CAL (Fig. 8c). At the surface, the relationship between the Fidas PM concentrations and simulated dust mass concentration is characterized by a regression slope of 0.56 ± 0.106 and a Pearson correlation coefficient of 0.383 (Fig. 5f). These statistics indicate substantially weaker correspondence than in dust case 2. Part of this discrepancy may arise from spatial representativeness, because the model profile used for comparison is located approximately 40 km from the measurement site, while clouds and precipitation during this event can vary considerably over such distances.

The largest upper-level backscatter discrepancy occurs where the dust layer overlaps with cloud, suggesting that aerosol–cloud interaction may contribute to the enhanced lidar signal. During period C1, ICON-ART underestimates the retrieved backscatter coefficient between approximately 2.6 and 4.4 km by a factor of 3.91 ± 1.66, even when non-spherical dust particles are assumed in the optical calculation. Two processes may contribute to this difference. First, the simulated dust loading may be too low. Second, the lidar signal may contain an additional contribution from liquid cloud droplets within the dust layer. ERA5 temperatures at the corresponding altitude remain above 0 °C, making liquid-water clouds physically plausible. The coexistence of dust and cloud droplets could increase the measured backscatter and would therefore complicate a direct interpretation of the lidar signal solely in terms of mineral-dust concentration. Because the available observations do not independently quantify the cloud contribution, however, the rela-

tive importance of insufficient simulated dust loading and cloud enhancement cannot be determined from this comparison alone. The lower-atmospheric discrepancy during C2 cannot be explained entirely by non-dust aerosol and therefore points to additional uncertainty in the simulated vertical dust distribution and cloud-related removal. Below approximately 3.2 km, ICON-ART backscatter is lower than the lidar retrieval by a factor of 7.48 ± 1.9. As in case 2, separating the lidar signal into dust and non-dust contributions reduces part of the difference, confirming that background aerosol contributes to the total backscatter. However, the dust-only lidar backscatter remains larger than the ICON-ART prediction, indicating that non-dust aerosol alone cannot account for the discrepancy. In contrast, the elevated dust layer between approximately 3.2 and 6.0 km exhibits much smaller differences between the observed and simulated profiles, suggesting that the model error is concentrated primarily in the lower part of the atmosphere. The surface and lower-level discrepancies should therefore not be attributed solely to excessive wet removal. Because clouds and precipitation were present throughout this period, the comparison is also sensitive to spatial displacement of simulated precipitation, differences in the vertical overlap among dust, cloud, and precipitation, and uncertainty in the resulting scavenging efficiency. The approximately 40 km separation between the model sampling location and the measurement site further limits a quantitative attribution of these differences to any single removal process. Case 3 therefore demonstrates that cloud-related processes and spatial representativeness must be considered explicitly when evaluating dust transport simulations under precipitating conditions.

3.1.3 Extreme Saharan dust outbreak (case 4)

The Saharan dust case 4 was observed at the KIT campus north from 16 March 2022 to 21 March 2022. This SAL was the most dense dust outbreak among all 4 cases with an AOD reaching values of 1.8 ± 0.07 at a wavelength of 550 nm in Karlsruhe (Kanngießer and Fiedler, 2026). Figure S5 shows the horizontal distribution of daily averaged aerosol optical depth (AOD) from MODIS satellite observations at a spatial resolution of $0.4° \times 0.4°$, for the period of 16–21 March 2021. During this time, Saharan dust originating in North Africa was transported toward Karlsruhe, Germany. The MODIS retrieval clearly depicts the presence of atmospheric SAL, exhibiting notably consistent spatial patterns. In particular, high AOD values over North Africa and the Middle East correspond well with established dust source regions. Figure 6 shows the time series of RCS for the polarized channel, cross-polarized channel, and LVDR from KASCAL measurements. The backscatter coefficients and particle depolarizations are not shown in this figure since their retrieval was impeded due to the presence of clouds from time to time. Figure 6 also shows the time series of ICON-ART predicted backscatter coefficients, particle number distributions, particulate matter concentrations, and ground level meteorological parameters (e.g. wind, precipitation, WS700). As can be seen from this figure, the Saharan dust layer arrived in Karlsruhe at 12:00 UTC on 16 March 2022 at an altitude between 2.0–3.5 km. Cloud cover was recorded after 00:00 UTC on 17 March 2022 with cloud base around 2.0 km. From 12:00 UTC of 17 March to 12:00 UTC of 18 March 2022, the presence of low level clouds and intermittent drizzle prevented the observation of the SAL by KASCAL. On midday of 18 March 2022, another SAL arrived in Karlsruhe at an altitude of 2.0–3.0 km and subsequently sunk to lower altitudes. This latter SAL was less intensive than that observed on 16 March 2022 as can be seen from the lower LVDR shown in panel (b) of this figure. The large particles observed at the surface by the Fidas 200 were not reproduced by the ICON-ART model, as shown in Fig. 6f. In addition, two periods (C1 and C2) are highlighted in this figure. These periods were used to further investigate dust properties measured by lidar and predicted by the ICON-ART model for different dust mass loadings. The evolution of the SAL over Karlsruhe for dust case 4 predicted by the ICON-ART model is shown in panel (d) of Fig. 6. This plot shows that two SALs arrived at Karlsruhe during these six days. The first SAL arrived at Karlsruhe at 00:00 UTC on 16 March 2022 with an initial dust layer height between 2.0–4.0 km and lasted nearly 3 d. This SAL was relatively dense until 00:00 UTC on 18 March 2022 and was washed out by precipitation on 00:00 UTC on 18 March 2022. Another less dense SAL arrived at Karlsruhe at 06:00 UTC on 21 March 2022 at an altitude of 2.0–3.0 km. The dust layer heights and their peak heights for both lidar measurement and ICON-ART prediction for this Saharan dust case are shown in Fig. 8d. The dust layer heights from ICON-ART prediction and lidar measurement show good agreement with each other. The vertical profiles of the backscatter coefficient from lidar retrieval and ICON-ART prediction for two selected periods indicated as C1 and C2 in Fig. 6 are shown on the right side of Fig. 6. For case C1, the vertical profile of backscatter coefficients predicted by ICON-ART agrees well with those retrieved from lidar measurements except for peak of backscatter coefficients at altitudes between 1.6 and 2.4 km. One possible reason for this phenomenon is that the ICON-ART model cannot resolve this small scale vertical aerosol distributions. For case C2, the backscatter coefficients predicted by ICON-ART are significantly lower than those observed below 3.2 km. One possible reason for this difference is that ICON-ART overestimates the washout effect by precipitation in this case.

Figure 7 presents the Linear Particle Depolarization Ratio (LPDR) versus lidar ratio retrieved from KASCAL for aerosol layers observed on different days for Saharan dust cases 1, 2, and 4. The lidar ratio for case 3 is not included due to the lack of reliable lidar data during cloud-free nighttime periods. For Cases 1 and 2, depolarization ratios of 0.28 ± 0.03 and 0.27 ± 0.02, and lidar ratios of 55 ± 10

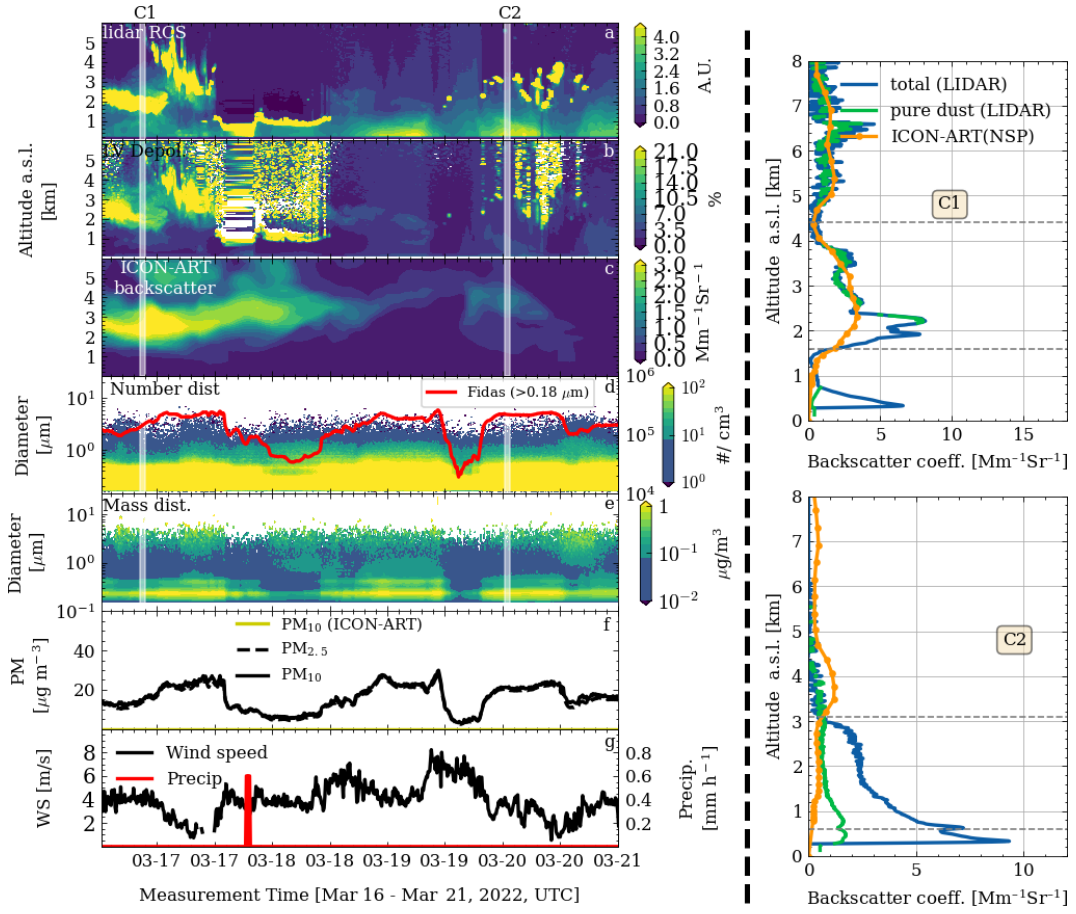


Figure 6. Time series of range corrected lidar signal for cross-polarized channel **(a)**, and Linear Volume Depolarization Ratio (LVDR) **(b)** from KASCAL measurements, backscatter coefficients predicted by ICON-ART **(c)**, particle number concentration **(d)**, particle mass size distribution from Fidas 200 **(e)**, particulate matter concentrations $PM_{2.5}$ and PM_{10} from the Fidas 200 and the lowest model level (150 m) of the ICON-ART simulation **(f)**, and ground level meteorological parameters (e.g. wind, precipitation, WS700) **(g)** from 16 to 21 March 2022 for case 4. The profiles of backscatter coefficients measured by the two lidars and predicted by ICON-ART model for C1 case (averaged profiles from 20:30 to 21:30 for lidar measurement and profile at 21:00 UTC for ICON-ART prediction on 16 March 2022) and for C2 case (averaged profiles from 00:30 to 01:30 for lidar measurement and profile at 01:00 UTC for ICON-ART prediction on 20 March 2022) are shown on the right side of this figure. C1 and C2 represent time periods used for a more detailed data analysis as shown in the right side of this figure.

and 57 ± 13 sr, respectively, were retrieved – values that are consistent with previous studies (Freudenthaler et al., 2009; Schuster et al., 2012; Cao et al., 2014). Case 4 reveals the presence of Saharan dust, continental aerosol layers with low depolarization characteristics, and mixtures of these aerosol types. The backward-trajectory analysis indicates that the low-depolarization aerosol layers were transported within the lower troposphere over continental Europe, suggesting contributions from regional and local aerosol sources in addition to long-range transported Saharan dust. On 16 March 2022, a dense dust layer was observed, characterized by a high depolarization ratio (0.32 ± 0.06) and a lidar ratio of 56 ± 11 sr. On 18 March, two distinct layers were identified: an upper dust layer (LPDR: 0.32 ± 0.04, lidar ratio: 36 ± 7 sr) and a lower low-depolarization aerosol layer (continental aerosol) (LPDR: 0.02 ± 0.003, lidar ratio: 38 ± 8 sr). On March 19, a mixed layer of Saharan dust and continental aerosols (LPDR: 0.11 ± 0.019, lidar ratio: 27 ± 7 sr) was observed below a continental aerosol layer (LPDR: 0.05 ± 0.004, lidar ratio: 49 ± 3 sr). By 20 March, the layers had mixed more uniformly, with LPDR and lidar ratio values of 0.1 ± 0.02 and 33 ± 13 sr, respectively.The temporal evolution of LPDR and lidar ratio indicates a progressive transition from a dust-dominated aerosol column to a more complex aerosol mixture. While the optical properties of the low-depolarization layers are consistent with aerosol types commonly associated with anthropogenic pollution and aged biomass-burning particles, the trajectory analysis suggests a substantial contribution from regional and local aerosol sources. The gradual decrease in LPDR and the emergence of intermediate

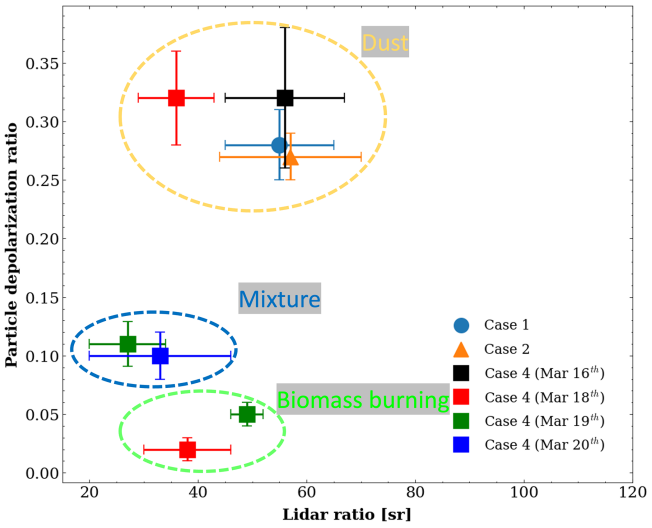


Figure 7. Linear Particle Depolarization Ratio (LPDR) versus lidar ratio retrieved from KASCAL for aerosol layers observed on different days across three Saharan dust cases. The lidar ratio for case 3 is not available due to the absence of reliable lidar measurements during cloud-free nighttime periods.

optical properties are consistent with increasing mixing between Saharan dust and regional aerosols during transport. This mixing results in intermediate depolarization values and variable lidar ratios, depending on the relative abundance of dust and low-depolarization layers in the column. These findings underscore the complexity of aerosol interactions and their evolving optical properties during long-range transport events involving multiple sources. The observed aerosol layering illustrates that realistic representation of aerosol mixing is essential for accurately simulating optical properties during long-range transport.

3.2 Statistical comparison of optical and microphysical properties

Table 2 summarizes the key optical parameters of Saharan dust retrieved from lidar and sun-photometer observations for all four investigated cases. As noted earlier, the lidar ratio for case 3 is not reported because no reliable lidar signals were available during cloud-free nighttime periods, and the single-scattering albedo (SSA) for this case is also excluded due to persistent cloud contamination. Overall, the retrieved optical properties exhibit values that are consistent with well-established characteristics of transported Saharan dust. In particular, the lidar ratios (LR), depolarization ratios, and SSA values fall within the range of previously reported measurements over North Africa and downwind regions (Freudenthaler et al., 2009; Schuster et al., 2012; Cao et al., 2014; Groß et al., 2011; Tesche et al., 2009a). This agreement suggests that our retrieval procedure accurately captures the microphysical and radiative signatures of mineral dust. Taken together, the close agreement with established climatological values and the physically consistent variability across cases provide confidence in the robustness of our observational dataset and support its relevance for evaluating dust representations in radiative transfer models and numerical simulations. Figure 8 shows the time series of dust base height, dust top height, and dust peak height for both lidar measurements and ICON-ART simulations. This figure shows that the dust arrival times predicted by the ICON-ART model agrees well with lidar measurements ($\pm$20 min) and in general for dust layer height ($\pm$50 m) in all 4 cases. However, ICON-ART also tends to overesimate the dust layer height (e.g. the first half of case 2 as shown in Fig. 8b). The remaining discrepancies between observations and ICON-ART predictions may be related to the following reasons: (1) Excessive vertical transport of dust in ICON-ART: During long-range transport, ICON-ART may transport dust particles to higher altitudes than observed, resulting in an overly elevated simulated dust layer and contributing to discrepancies in the modeled vertical dust distribution. (2) Low lidar sensitivity to elevated dust layers: At higher altitudes, the lidar measurements are characterized by a relatively low signal-to-noise ratio because of the weaker aerosol backscatter signal. This increases the uncertainty in detecting and quantifying tenuous dust layers aloft and may partly explain the differences between the modeled and observed dust vertical distributions.

Figure 9 shows the correlation of dust base heights, dust peak heights, and dust top heights from lidar measurements and ICON-ART predictions for the four Saharan dust cases. Across the four cases, 51 %, 61 %, and 61 % of the paired dust-base, dust-peak, and dust-top heights, respectively, fall within the $\pm$25 % agreement band around the 1 : 1 relationship, indicating that substantial discrepancies remain despite the model's representation of the broad event evolution. To be clear, good agreement in dust layer heights can be seen for cases 1, 3, and 4 but not for case 2 as discussed before. In general, the ICON-ART model predicts dust arrival times and dust layer heights very well if considering the spatial resolution of the ICON-ART model (26.0 km horizontally).

3.3 Model performance under different resolutions and initialization

The EXP-5d and RI-EXP-1d simulations were conducted to investigate the effects of meteorological reinitialization and grid resolution on Saharan dust predictions. To evaluate the meteorological fields underlying these predictions, simulated temperature, wind speed, and wind direction profiles were compared with radiosonde observations at eight meteorological stations. Temperature profiles characterize the thermal structure relevant to atmospheric stability, while wind profiles constrain the horizontal transport of dust at different altitudes. Figure 10 shows station-mean model-minus-observation biases between 1000 and 300 hPa for the 26

Table 2. Overview of optical parameters of Saharan dust determined from lidar data, sun photometer measurements, and ICON-ART simulations for all four Saharan dust cases.

Parameter	λ [nm]	Case 1	Case 2	Case 3	Case 4	Average	Reference
BSC. (Mm^{-1} sr^{-1})	355	0.95 ± 0.23	0.91 ± 0.43	1.52 ± 0.31	3.17 ± 2.48	1.64 ± 0.70	this work (lidar)
BSC. ($Mm^{-1}sr^{-1}$)	355	0.71 ± 0.37	1.15 ± 0.41	0.73 ± 0.30	0.77 ± 0.73	0.84 ± 0.47	this work (ICON-ART)
LPDR	355	0.28 ± 0.03	0.27 ± 0.02	0.31 ± 0.04	0.30 ± 0.03	0.29 ± 0.03	0.252 ± 0.03 (Haarig et al., 2017)
LR (sr)	355	46 ± 10	57 ± 13		55 ± 10	53 ± 11	48 ± 8 (Haarig et al., 2022)
AOD	340	0.21 ± 0.12	0.33 ± 0.12	0.52 ± 0.14	0.80 ± 0.42	0.47 ± 0.20	this work (sun photometer)
AOD	500	0.25 ± 0.11	0.39 ± 0.12	0.57 ± 0.12	0.91 ± 0.42	0.53 ± 0.19	this work (sun photometer)
AOD	550	0.17 ± 0.09	0.36 ± 0.22	0.24 ± 0.10	0.18 ± 0.06	0.24 ± 0.12	this work (ICON-ART)
AOD	1020	0.30 ± 0.11	0.41 ± 0.14	0.69 ± 0.12	1.01 ± 0.43	0.60 ± 0.20	this work (sun photometer)
SSA	439	0.92 ± 0.03	0.90 ± 0.27		0.93 ± 0.01	0.91 ± 0.10	0.91 (Müller et al., 2012)
SSA	870	0.93 ± 0.04	0.95 ± 0.23		0.95 ± 0.01	0.94 ± 0.09	0.86–0.98 (Zo and Shin, 2019)

BSC: backscatter coefficient; Exc: extinction coefficient; LR: lidar ratio; LPDR: linear particle depolariization ratio. AOD: Aerosol optical depth, SSA: single scatter albedo.

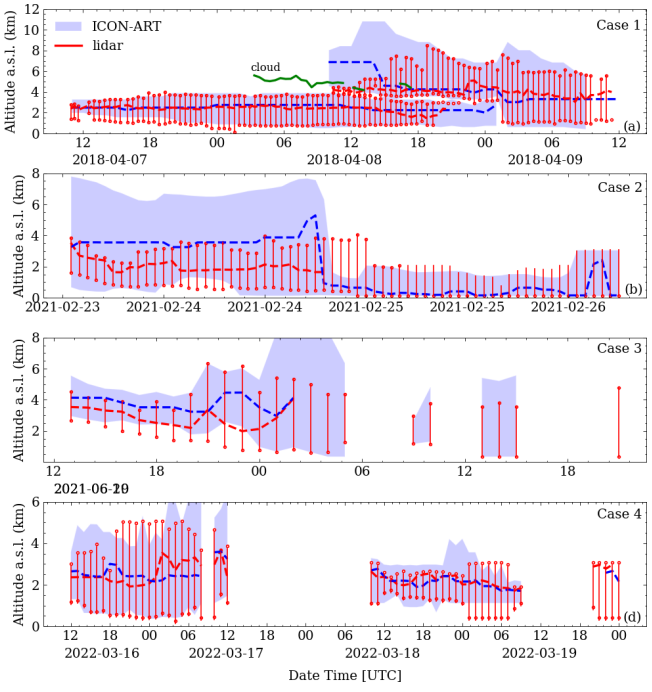


Figure 8. Time series of Saharan dust layer heights (vertical extend) and their peak heights (heights of maximum backscatter coefficients, indicated as red (lidar) and blue (ICON-ART) solid line) from both lidar measurements (red bars) and ICON-ART predictions (light blue area) for cases 1–4.

and 1 km simulations at 12:00 UTC on 22 and 25 February 2021. Errors were calculated separately at each station before averaging, and the error bars indicate ±1 standard deviation across valid stations. Complementary full-column statistics were calculated individually for each station and then averaged with equal station weights to obtain the time series in Fig. S6. The two experiments show similar performance early in the simulation, whereas larger differences emerge later. By 25 February, EXP-5d exhibits pronounced wind-direction biases near 500 hPa and in parts of the lower troposphere, together with larger wind-speed biases at several levels; these departures are generally reduced in RI-EXP-1d (Fig. 10). The full-column statistics support this improvement. At 12:00 UTC on 25 February, daily reinitialization reduces the station-mean temperature RMSE from 1.89 to 1.07 °C and wind-speed RMSE from 4.61 to 2.18 $m\,s^{-1}$ at 13 km, while the mean wind-speed correlation increases from 0.61 to 0.84. The mean wind-direction RMSE decreases from 53.2 to 32.5°, accompanied by an increase in the mean circular correlation from 0.43 to 0.75. Although RI-EXP-1d yields higher correlation coefficients, the near-unity full-column temperature correlations primarily reflect the shared vertical temperature structure and should therefore be interpreted alongside RMSE and bias. Increasing horizontal resolution does not consistently improve agreement with the radiosonde observations. The 26 and 13 km simulations generally perform better than the 2 and 1 km simulations in these station-averaged diagnostics, particularly for RI-EXP-1d (Fig. S6). One possible explanation is that transferring meteorological fields from the parent domains to the finer nests introduces interpolation errors or adjustments as the flow adapts to the finer grids and their representation of topography. Such effects could contribute to the temperature and wind discrepancies in the nested simulations, although their contribution has not been isolated here. These meteorological errors could, in turn, affect predicted dust transport pathways and concentrations, potentially limiting the benefits of increased horizontal resolution. Nevertheless, the improved temperature and wind profiles in RI-EXP-1d provide observational support for improved meteorology as a contributor to its better dust predictions.

The lidar-observed and ICON-ART-simulated evolution of Saharan dust over KIT-CN for the EXP-5d and RI-EXP-1d experiments, using the 26 km nest of the global configuration and the 1 km nest of the limited-area model (LAM) configuration, is shown in Fig. 11. Results from the 13 and 2 km simulations are shown in Fig. S7. It has to be noted

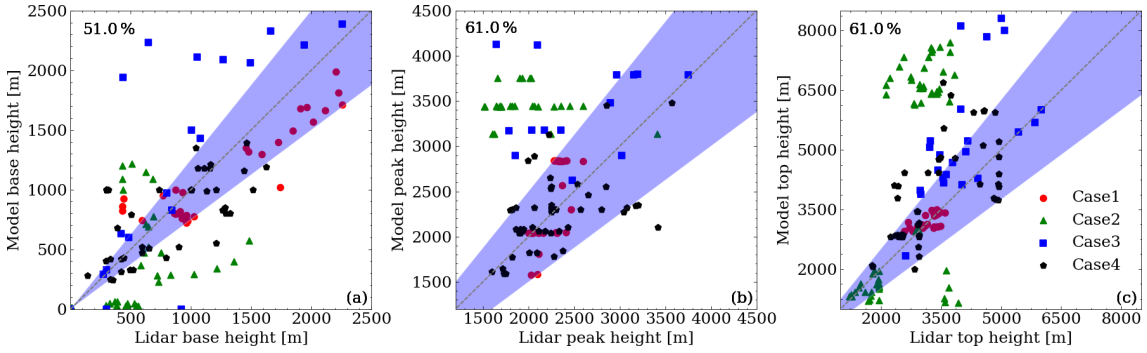


Figure 9. Correlation of dust base heights **(a)**, dust peak heights **(b)**, and dust top heights **(c)** from lidar measurements and ICON-ART simulations for all 4 Saharan dust cases.The blue-shaded area indicates slopes between 0.75 and 1.25 and the number shown in the left upper corner is the percentage of data points within this blue-shaded area.

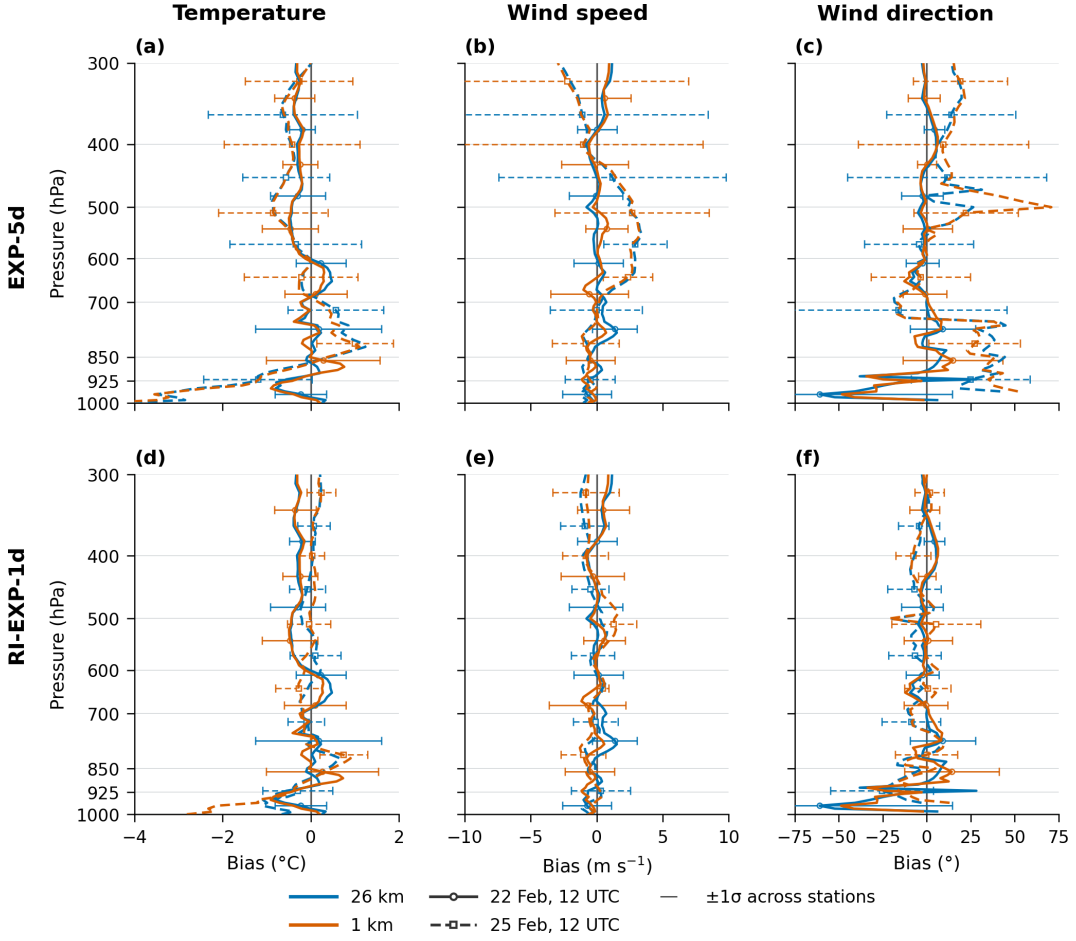


Figure 10. Vertical profiles of model-minus-radiosonde biases in temperature **(a, d)**, wind speed **(b, e)**, and wind direction **(c, f)** for EXP-5d (top row) and RI-EXP-1d (bottom row). Blue and orange indicate the 26 and 1 km simulations, respectively; solid and dashed lines indicate 22 and 25 February 2021 at 12:00 UTC. Errors are calculated separately at each station before averaging across the valid stations among the eight selected sites.

that the effective resolution of resolved processes by the model is still around 5–6 horizontal resolution. At the synoptic scale, both experiments reproduce the timing of the Saharan dust outbreak and its large-scale transport pathway from North Africa toward Central Europe, whereas more pronounced differences emerge in the vertical dust distribution and near-surface concentrations. Compared with the continuous 5 d forecast (EXP-5d), the daily re-initialized simulations (RI-EXP-1d) provide a closer representation of the observed dust-layer heights, vertical backscatter structure, and near-surface PM_{10} variability. In particular, across all model resolutions, the correlation between simulated and observed near-surface PM_{10} concentrations increases from $R = 0.65$–0.69 in EXP-5d to $R = 0.86$–0.88 in RI-EXP-1d, while the RMSE decreases by approximately one third.

The improvement in RI-EXP-1d is consistent with a reduction in accumulated forecast errors through daily re-initialization as shown in Figs. 10 and S6, although the mechanism differs between the global and limited-area simulations. In the global simulations, re-initialization updates both the meteorological state and the dust fields, which can introduce discontinuities in the simulated dust distribution at the re-initialization times. In contrast, the limited-area model (LAM) simulations are not directly re-initialized internally and are affected primarily through the updated lateral boundary conditions. Consequently, the improvement in the LAM simulations is more directly associated with the repeated refresh of the meteorological forcing and boundary conditions. By constraining the large-scale circulation, frontal evolution, and associated vertical motions more frequently, daily re-initialization limits the accumulation of meteorological forecast errors and thereby improves the simulated transport and near-surface evolution of the dust plume. Despite the improved meteorological forcing, differences between the simulations and observations remain. This is expected because the re-initialization procedure only constrains meteorological variables, while no corresponding assimilation is available for mineral dust tracers. Consequently, uncertainties associated with dust emission, deposition, and aerosol transport processes continue to evolve freely within the model. These uncertainties can accumulate during transport from the Saharan source regions and may contribute to discrepancies in both dust concentration and vertical distribution, even when the meteorological conditions are well represented.

The influence of horizontal resolution on the overall dust evolution is relatively modest, whereas a clearer improvement emerges when higher resolution is combined with daily updated boundary conditions. The general structure of the time–height backscatter cross sections remains similar across the different resolutions, indicating that increasing resolution alone does not substantially alter the large-scale dust transport. Resolution-dependent differences become more apparent in the near-surface PM_{10} concentrations and in the detailed vertical dust structure (Fig. 12), with the 26/13 and 2/1 km simulations forming two relatively similar groups. These differences occur both within the boundary layer and in the elevated dust layers, but their magnitude remains limited in EXP-5d. In contrast, the resolution dependence becomes more evident in RI-EXP-1d: the higher-resolution simulations better reproduce the observed vertical dust distribution within the boundary layer, especially below 800 m (Fig. 12b, d), and generally reduce the simulated backscatter in the upper dust layers at 6–8 km (Fig. 12a,c). However, the radiosonde comparisons show that the 2 and 1 km simulations generally exhibit larger temperature and wind-profile errors than the 26 and 13 km simulations, particularly in RI-EXP-1d (Fig. S6). These meteorological discrepancies could affect dust advection and dispersion and may contribute to higher simulated dust concentrations in the finer nests. This remains a possible contribution rather than a demonstrated cause, since larger meteorological errors do not necessarily imply a positive dust-concentration bias. These results suggest that increasing horizontal resolution alone provides only limited improvement, whereas its benefit becomes more apparent when the limited-area simulations are driven by daily updated lateral boundary conditions. The improved boundary forcing constrains the large-scale dust transport, while the finer grid provides a more detailed representation of the vertical redistribution of dust, particularly within the boundary layer.

Overall, the results indicate that forecast strategy has a stronger influence on the simulated dust evolution than horizontal resolution alone. Daily re-initialization, through regularly updated meteorological forcing and lateral boundary conditions, substantially reduces the accumulation of forecast errors and improves the representation of dust transport. Increasing horizontal resolution produces comparatively smaller changes in the overall dust distribution, but its benefits become more evident in the RI-EXP-1d simulations, particularly in resolving the detailed vertical structure of dust within the boundary layer. These results suggest that higher resolution is most effective when combined with more accurate and frequently updated large-scale forcing. The comparison between the ground-based lidar observations and the ICON-ART simulations at different horizontal resolutions for period C1 indicates that the model reasonably reproduces the observed dust layer below approximately 2.6 km. However, all ICON-ART simulations systematically overestimate the backscatter coefficient between approximately 2.6 and 8 km. To further investigate this discrepancy, we additionally compared the ground-based lidar observations with CALIPSO retrievals, as shown in Fig. 13. The closest distance between the CALIPSO ground track and the KIT-CN observation site was approximately 20 km. Figure 13 shows the latitude–height cross section of the aerosol backscatter coefficient from the CALIPSO retrieval at 532 nm and the corresponding ICON-ART simulations at horizontal grid spacings of 26 km and 1 km for both EXP-5d (panels b–c) and RI-EXP-1d (panels e–f) experiments. The results from the 13 and 2 km simulations are provided in Fig. S8. This

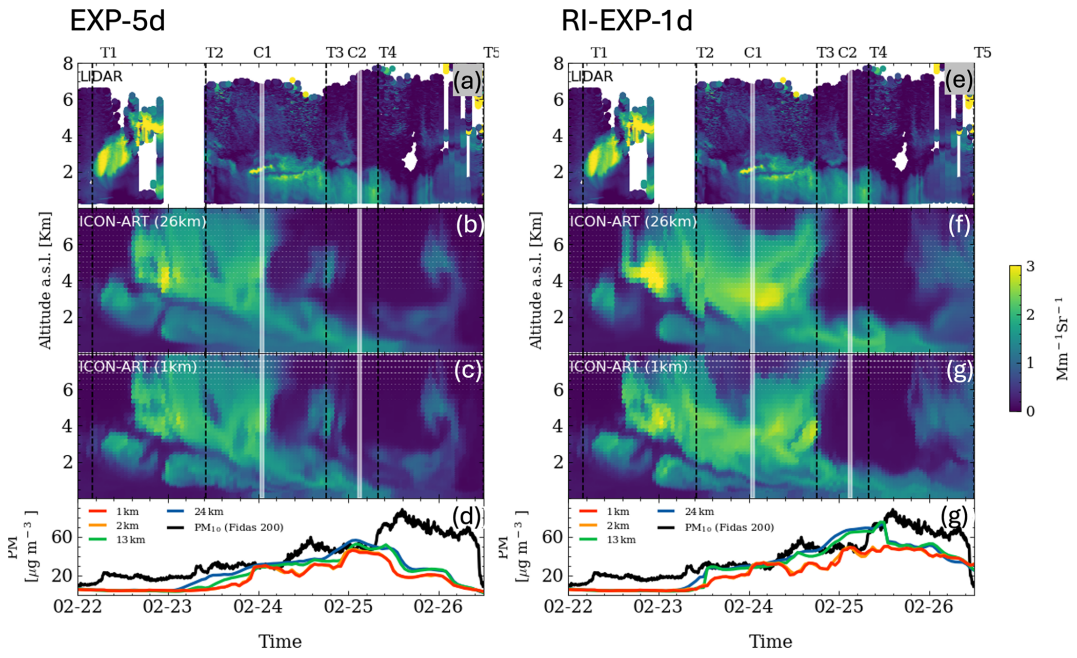


Figure 11. Time–height cross section of lidar backscatter coefficient **(a)**. Corresponding ICON-ART backscatter coefficient simulated at horizontal grid spacings of 26 km, and 1 km, respectively **(b–c)**. Time series of surface PM concentration measured by Fidas 200 (black) and simulated by ICON-ART **(f)** from 22 to 26 February 2021. Panels **(f)–(g)** are the same as panels **(b)–(d)**, but for the RI-EXP-1d experiment.

figure show that ICON-ART model shows agreement with CALIPSO retrievals in term of dust height and dust structure with RMSE = 0.40–0.45 $Mm^{-1}\,sr^{-1}$ and Bias = 0.21–0.29 $Mm^{-1}\,sr^{-1}$. The comparison of EXP-5d experiments with RI-EXP-1d experiments shown in Fig. S9 illustrates the impact of initialization conditions on simulation result. In contrast to EXP-5d (left), where no clear resolution dependence is observed, RI-EXP-1d (right) exhibits a pronounced resolution dependence, especially between 7 and 8 km altitude. In this altitude range, the kilometre-resolution RI-EXP-1d simulations show reduced backscatter coefficients compared with the coarser-resolution simulations, leading to better agreement with the CALIPSO retrievals. This suggests that, for RI-EXP-1d, increasing the horizontal resolution improves the representation of the upper part of the dust layer, while this improvement is not evident in the EXP-5d simulations.

Figure 14 presents vertical profiles of the aerosol backscatter coefficient from ground-based lidar observations and the 1 km ICON-ART simulations for the EXP-5d and RI-EXP-1d experiments at 355 nm (left), together with the corresponding profiles from CALIPSO retrievals and the 1 km ICON-ART simulations at 532 nm (right). The comparison reveals a clear wavelength-dependent behavior in the model performance. At 355 nm, ICON-ART generally overestimates the aerosol backscatter coefficient relative to the KASCAL retrievals, particularly between 5.2 and 6.6 km, where the mean simulated-to-observed ratio is 5.08 ± 5.56. At 532 nm, the simulated profile shows substantially better agreement with CALIPSO observations, with a mean ratio of 1.34 ± 0.58 over the same altitude range. This suggests that the simulated aerosol optical properties exhibit a stronger spectral dependence than indicated by the lidar observations. The contrasting model performance at 355 and 532 nm points to a potential bias in the particle size distribution represented in ICON-ART. In particular, an excessive contribution from relatively small and intermediate-sized particles would enhance backscattering more strongly at shorter wavelengths, leading to a larger simulated backscatter coefficient at 355 nm relative to 532 nm. This interpretation is consistent with the comparison against the Fidas 200 measurements (cf. Fig. S10), which shows that ICON-ART underestimates the abundance of coarse particles while overestimating particles in the intermediate size range. Because coarse particles generally exhibit a weaker wavelength dependence of their optical properties than smaller particles, this shift in the simulated size distribution toward smaller sizes can result in an excessively strong spectral dependence of the aerosol backscatter coefficient.

Figure 15 compares the ICON-ART dust AOD with the AERONET coarse-mode AOD for the EXP-5d and RI-EXP-1d simulations at four horizontal grid spacings. ICON-ART captures the variability in AERONET coarse-mode AOD reasonably well across all four horizontal grid spacings, although the agreement depends more strongly on the reinitialization than on grid resolution. For a given configuration, the correlation coefficients and other statistical metrics remain largely insensitive to changes in horizontal grid

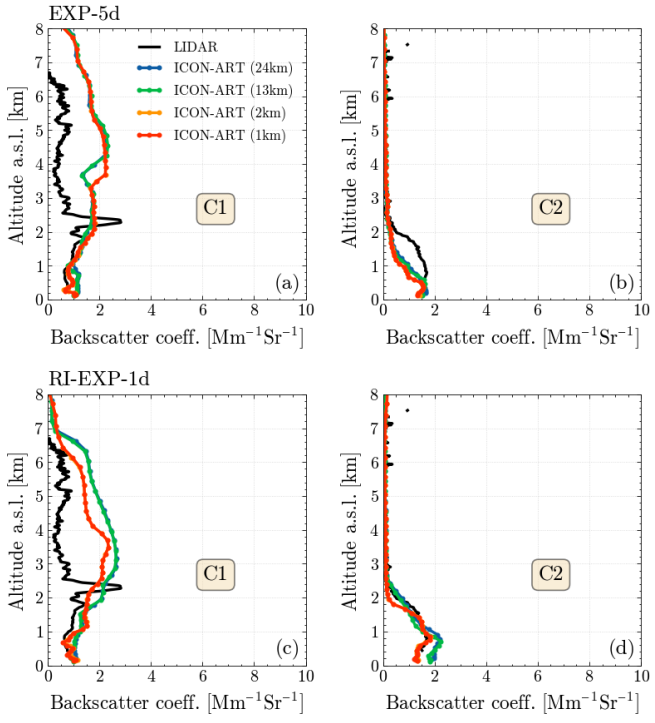


Figure 12. Profiles of pure dust backscatter coefficients measured by the lidar and predicted by ICON-ART model for case C1 (*g*: averaged profiles from 00:30 to 01:30 for lidar measurement and profile at 01:00 UTC for ICON-ART prediction on 24 February 2021) and for case C2 (*h*; averaged profiles from 02:30 to 03:30 for lidar measurement and profile at 03:00 UTC for ICON-ART prediction on 25 February 2021).

spacing from 26 to 1 km. The standard EXP-5d simulations yield correlations of $r = 0.584$–0.588 and regression slopes of 0.790–0.811. The slopes of approximately 0.8 indicate that the model increasingly underestimates AOD as the observed AOD increases, despite the small mean biases (−0.009 to 0.009). RI-EXP-1d increases the correlations to $r = 0.642$–0.656 and brings the regression slopes closer to unity (0.972–1.045), indicating an improved representation of the observed AOD magnitude and variability. However, this improvement is accompanied by positive mean biases of 0.027–0.042 and does not lead to a systematic reduction in RMSE. Among the RI-EXP-1d simulations, the 1 km simulation shows the closest agreement, with $r = 0.656$, a slope of 0.972, an RMSE of 0.128, and a mean bias of 0.027. Overall, daily reinitialization improves the correlation and regression slope of simulated dust AOD relative to AERONET observations, whereas increasing horizontal resolution provides comparatively limited additional benefit. The remaining positive biases and the lack of a consistent reduction in RMSE indicate that improved representation of AOD variability does not necessarily translate into smaller absolute errors.

These optical comparisons should, however, be interpreted in light of uncertainties in the particle size distribution (PSD) assumed in ICON-ART, as the PSD directly affects the conversion of simulated aerosol mass into optical properties. This issue is particularly relevant to the coarse mode: ICON-ART substantially underestimates both PM_{10} and coarse-particle mass and underrepresents the pronounced contribution of particles larger than approximately 5 µm evident in the observations, as shown in Fig. S10 and reported in previous studies (Hoshyaripour et al., 2019). Consequently, part of the remaining AOD discrepancy may arise from uncertainties in the assumed PSD and the associated optical properties, in addition to the underestimated coarse-aerosol burden. The persistence of similar AOD statistics across resolutions therefore suggests that the dominant discrepancies are related to aerosol representation, including the coarse-particle size distribution and mass, and/or model–observation differences, rather than spatial resolution alone.

Figure 16 presents the time series of ground-level aerosol mass size distributions (dM / dlnD) measured by the Fidas 200 optical particle spectrometer and the corresponding dust mass size distributions simulated by ICON-ART at horizontal resolutions of 26, 13, 2, and 1 km. The model results from both the continuous 5 d forecast experiment (EXP-5d) and the daily re-initialized forecast experiment (RI-EXP-1d) are shown. Both the observations and simulations indicate that the dust particles reached the surface during the period from approximately 10:00 UTC on 23 February to 12:00 UTC on 26 February 2021. During this period, enhanced concentrations of coarse-mode particles were observed by the Fidas 200 instrument and reproduced by ICON-ART, consistent with the downward transport of mineral dust into the boundary layer. The RI-EXP-1d experiment generally shows better agreement with the observations in terms of both the timing and duration of the surface dust event. In contrast, the EXP-5d simulations, particularly at 2 and 1 km resolution, tend to underestimate the duration of the near-surface dust occurrence and simulate a shorter period during which the SAL remains in contact with the surface. These larger discrepancies in the kilometer-scale EXP-5d simulations may partly reflect errors in the meteorological background. The radiosonde evaluation in Figs. 10 and S6 shows that EXP-5d generally develops larger temperature and wind-profile errors than RI-EXP-1d as the simulation progresses, while the finer grids do not consistently improve meteorological agreement. This result suggests that errors accumulated in the meteorological fields during the continuous 5 d forecast can affect the representation of boundary-layer processes and vertical dust transport. Deviations in the simulated wind field, together with possible errors in boundary-layer depth or vertical mixing, could contribute to differences in the timing and persistence of dust reaching the surface. The differences among model resolutions further suggest that the surface concentration of transported dust is sensitive to mesoscale and local-scale dynamical processes. While the coarser simulations re-

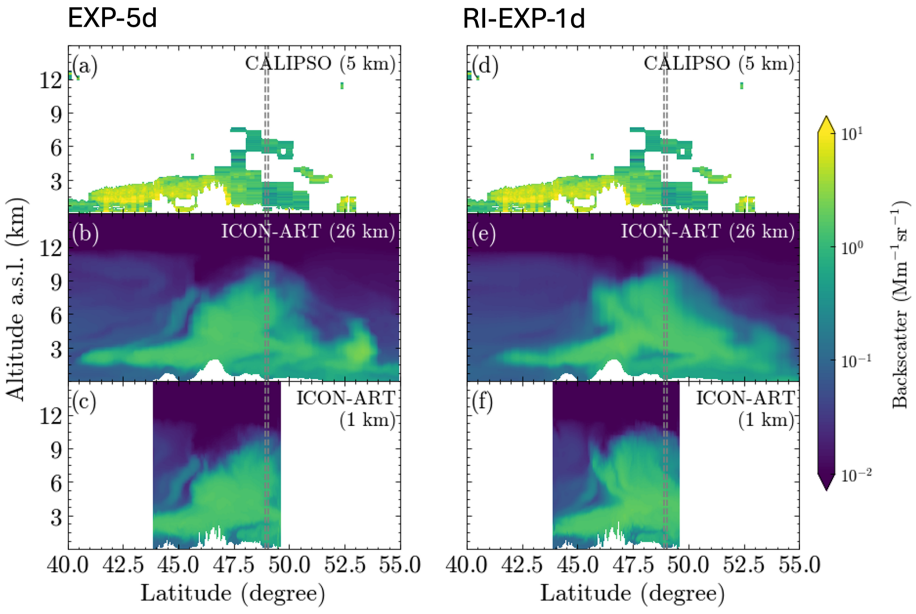


Figure 13. Latitude height of backscatter coefficient at 532 nm from CALIPSO retrieval **(a)** and ICON-ART simulation for horizontal grid spacings of 26 km and 1 km, respectively **(b–c)**. Panels **(e)–(f)** are the same as panels **(b)–(c)**, but for the RI-EXP-1d experiment. The data was sampled at 13:00 UTC on 23 February 2021.

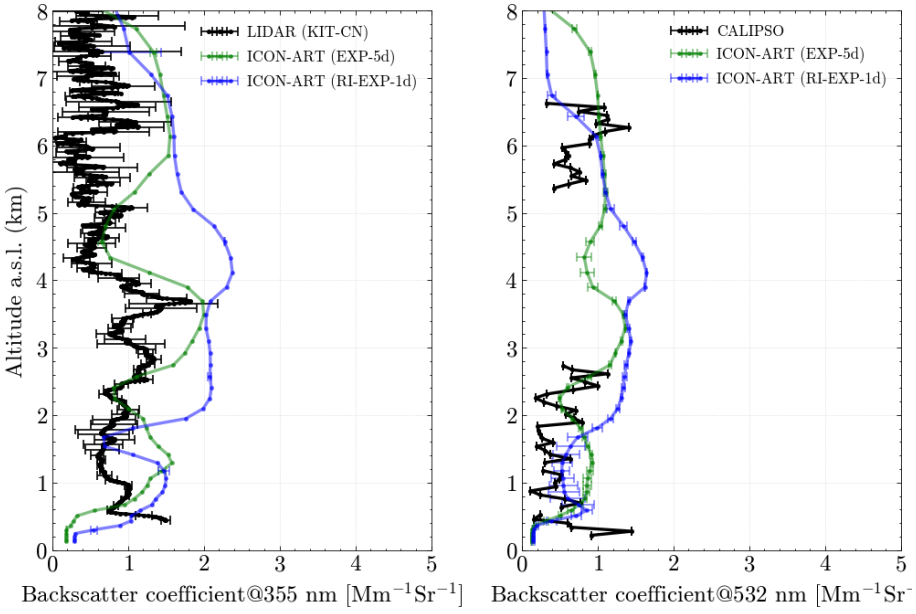


Figure 14. Vertical profiles of the aerosol backscatter coefficients from ground-based lidar observations and ICON-ART simulation (1 km) for both EXP-5d and RI-EXP-1d experiments at 355 nm (left) as well as vertical profiles of the aerosol backscatter coefficient from CALIPSO retrievals and the ICON-ART simulation (1 km) for both EXP-5d and RI-EXP-1d experiments at 532 nm. The data was sampled at 13:00 UTC on 23 February 2021.

produce the overall temporal evolution of the dust event, the kilometer-scale simulations can represent finer-scale structures in the boundary layer and topographically induced circulations that influence the vertical redistribution of dust. However, inaccuracies in the meteorological forcing, potentially compounded by adjustments associated with nesting, may limit these benefits and contribute to the larger surface-dust discrepancies in the 2 and 1 km EXP-5d simulations. Consequently, the benefits of increased spatial resolution become most evident when combined with improved meteo-

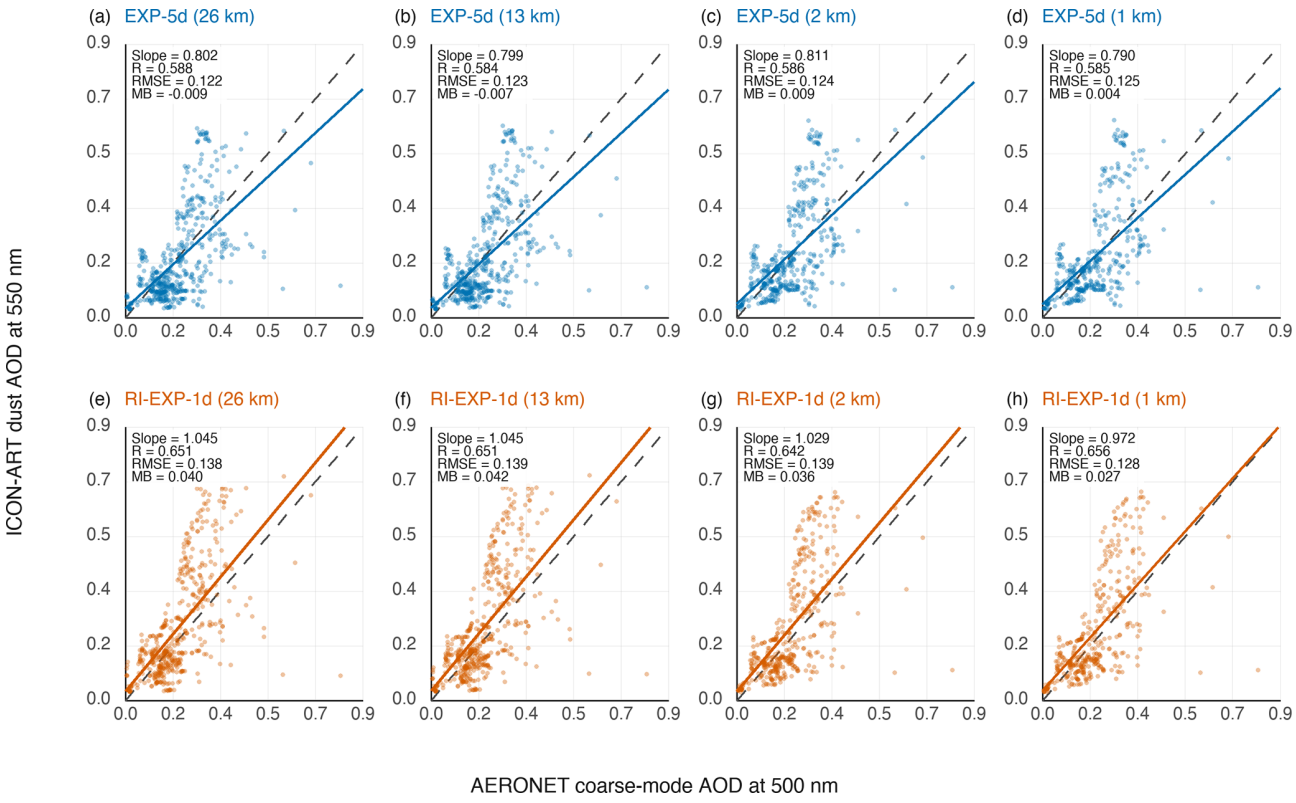


Figure 15. Comparison of AERONET coarse-mode AOD and ICON-ART-simulated dust AOD for the EXP-5d **(a–d)** and RI-EXP-1d **(e–h)** simulations at horizontal grid spacings of 26, 13, 2, and 1 km. The analysis is restricted to the innermost model domain, which contains 17 AERONET sites. Solid lines represent the least-squares linear regressions, and dashed lines indicate the 1 : 1 relationship. The reported statistics are the regression slope, Pearson correlation coefficient (r), root-mean-square error (RMSE), and mean bias (MB; model minus observation).

rological initialization, as demonstrated by the RI-EXP-1d experiment. Overall, the results suggest that an accurate representation of both meteorological conditions and mesoscale transport processes is essential for reproducing the timing, duration, and size-dependent characteristics of surface Saharan dust concentrations.

The averaged aerosol/dust size distributions during the three periods (P1, P2, and P3 in Fig. 16) are shown in Fig. S10. Overall, the ICON-ART simulations reproduce the general shape and temporal evolution of the observed size distributions during the Saharan dust event. However, systematic biases are evident across all periods. The model tends to overestimate the mass concentration for particle diameters between approximately 0.5 and 2 µm, while underestimating the mass concentration for particles larger than 2 µm. A similar conclusion was reached by Ratcliffe et al. (2025), who showed that additional processes counteracting the rapid sedimentation of coarse dust particles are required for climate models to reproduce observations. This behaviour suggests that the simulated dust size distribution is shifted toward smaller particle sizes compared with the observations. The underrepresentation of coarse particles may be related to excessive removal of large dust particles during transport through gravitational settling and dry deposition, insufficient emission of coarse-mode dust at the source regions, or uncertainties in the prescribed dust size distribution. Consequently, the model retains too much mass in the accumulation mode while underestimating the contribution of coarse-mode particles at the observation site. The persistence of this bias in both the EXP-5d and RI-EXP-1d experiments indicates that the discrepancies in the size distributions are likely associated with uncertainties in dust microphysical processes and size-dependent deposition rather than meteorological initialization. While the daily re-initialization improves the representation of the dust-layer structure and transport pathways, it has a relatively limited impact on the simulated surface size spectra. These results suggest that further improvements in the parameterization of dust emission, sedimentation, and deposition processes are required to accurately reproduce the observed particle size distributions during long-range Saharan dust transport events.

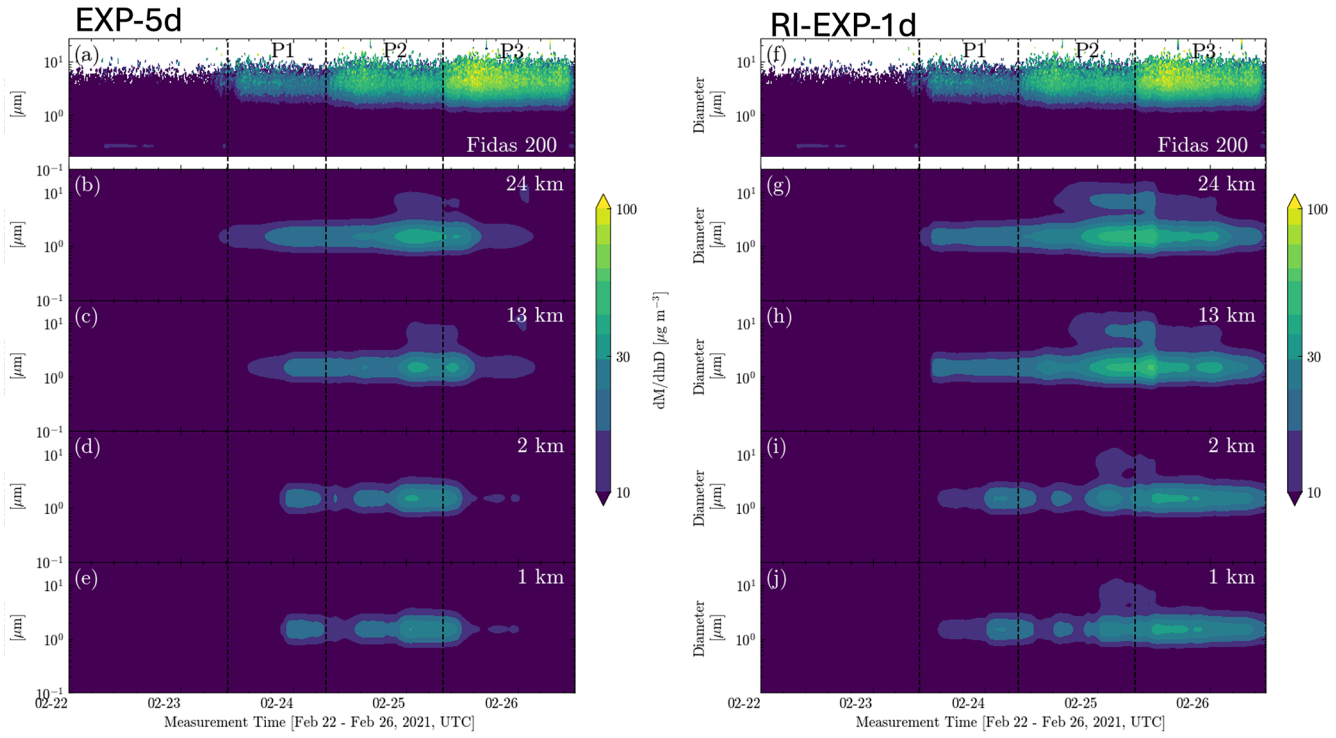


Figure 16. Time series of ground-level aerosol mass size distributions (dM / dlnD) measured by the Fidas 200 optical particle spectrometer **(a)** and simulated dust mass size distributions from ICON-ART at horizontal resolutions of 26, 13, 2, and 1 km **(b–e)**. Results from EXP-5d experiment **(b–e)** and RI-EXP-1d experiment **(g–j)** are presented for the Saharan dust event of 21–25 February 2021.

4 Discussion

The comparison of observations with ICON-ART simulations for four Saharan dust events and two sensitivity experiments provides insight into the main sources of model-observation discrepancies. Three main findings emerge. First, the large-scale transport pathway and plume arrival time are reproduced consistently across all model resolutions and meteorological initialization strategies, with a mean arrival-time difference of approximately 20 min even at 20 km horizontal resolution. Second, the aerosol loading and vertical distribution of dust are strongly influenced by both meteorological initialization and horizontal resolution, with the best agreement achieved only when both are improved simultaneously. Third, the particle size distribution and some systematic features of the optical properties remain largely unchanged across all experiments, suggesting that these persistent discrepancies originate from the aerosol representation rather than from the transport itself.

The improvement in the simulated vertical dust structure is one of the main findings of this study. Compared with the continuous 5 d forecast (EXP-5d), the daily re-initialized forecast (RI-EXP-1d) increases the correlation between simulated and observed near-surface PM_{10} concentrations from $R = 0.65$–0.69 to $R = 0.86$–0.88 across all model resolutions, while reducing the RMSE by approximately one third. RI-EXP-1d also increases the correlation between simulated and observed AOD from $R = 0.29$–0.31 to $R = 0.41$–0.42 (Table S1). These results show that daily reinitialization provides a better representation of both surface dust concentrations and column-integrated aerosol loading. This sensitivity to meteorological forcing agrees with previous studies showing that Saharan dust outbreaks contribute to short-range forecast uncertainty over Europe (Hermes et al., 2024) and that updated meteorological analyses improve aerosol forecast skill in operational forecasting systems (Benedetti et al., 2009). The radiosonde comparisons provide direct evidence of the meteorological improvement: RI-EXP-1d generally reduces temperature and wind-profile errors relative to EXP-5d, with larger differences emerging later in the simulation (Figs. 10 and S6). The 2 and 1 km simulations do not consistently outperform the coarser grids in these meteorological diagnostics, suggesting that errors in the meteorological background may limit the benefits of finer resolution for dust prediction. The improvement is not solely attributable to increased horizontal resolution. Similar improvements from EXP-5d to RI-EXP-1d are found at both coarse (26 and 13 km) and convection-permitting (2 and 1 km) resolutions, supporting reduced accumulation of meteorological forecast errors as a contributor to the improved timing and duration of near-surface dust events. Higher resolution provides an additional benefit, with sharper dust-layer

boundaries and reduced overestimation of elevated dust concentrations (Figs. 10 and 12), potentially reflecting a more detailed representation of circulations and vertical exchange between the free troposphere and the boundary layer. These findings are consistent with previous studies demonstrating that convection-permitting simulations improve the representation of dust-related vertical transport processes associated with convective downdrafts and cold pools (Marsham et al., 2011; Heinold et al., 2013). However, higher resolution alone does not compensate for deficiencies in the meteorological forcing. In the EXP-5d simulations, the 1 and 2 km experiments underestimate the duration of the near-surface dust event more strongly than the coarser-resolution simulations, possibly because errors in the meteorological background affect the resolved boundary-layer transport. These results suggest that meteorological initialization and horizontal resolution can provide complementary improvements, with the benefits of finer resolution becoming more apparent when combined with daily reinitialization.

At first glance, the backscatter-profile statistics appear inconsistent with the improvements obtained for near-surface PM_{10}. The normalized mean bias of the lidar-model comparison is smaller for EXP-5d (5.9 %–6.5 %) than for RI-EXP-1d (38 %–50 %), whereas RMSE and correlation remain similar in both experiments ($R \approx 0.37$–0.41) (Table S1). This behaviour is most likely explained by compensating errors rather than improved model performance. A continuous forecast may therefore produce a smaller overall bias if underestimation at one altitude compensates for overestimation elsewhere, without improving the vertical profile itself. This interpretation is supported by the nearly unchanged RMSE between EXP-5d and RI-EXP-1d. Similar limitations of profile-integrated bias metrics have been reported previously, and profile-resolved statistics are generally recommended for evaluating vertically resolved aerosol simulations (Binietoglou et al., 2015). Consequently, the backscatter results do not contradict the improvements in vertical dust transport but instead indicate that improved meteorological forcing and resolution improve the vertical redistribution of dust without correcting the persistent overestimation of elevated aerosol layers.

The overestimation of elevated dust layers forms part of a broader pattern that is largely unaffected by either model resolution or meteorological initialization. ICON-ART overestimates the backscatter coefficient at 355 nm (KASCAL) but show agreement with the backscatter coefficient at 532 nm (CALIPSO). This wavelength-dependent behaviour is consistent with ICON-ART underestimating the abundance of coarse particles while overestimating intermediate-sized particles. This interpretation is independently supported by the particle mass size distributions measured by the Fidas 200 (Figs. 15 and S9). ICON-ART consistently overestimates particles between approximately 0.5 and 2 µm while underestimating particles larger than 2 µm, and these biases remain nearly unchanged in both EXP-5d and RI-EXP-1d. Since meteorological re-initialization substantially improves the timing and duration of surface dust events without affecting the particle size distribution, the remaining discrepancy likely reflects limitations in the representation of the emitted size distribution and the size-dependent removal of coarse particles, potentially through sedimentation and dry deposition during long-range transport. This interpretation is consistent with previous studies. Ratcliffe et al. (2025) showed that additional processes are required to maintain coarse dust during atmospheric transport, while Adebiyi and Kok (2020) demonstrated from a global synthesis of in-situ observations that current models remove coarse dust too efficiently. The present study extends these findings to long-range Saharan dust transport over Europe using both remote sensing and in-situ observations.

Wet deposition represents another potential source of uncertainty, particularly during case 3. Observations show that moderate precipitation efficiently removed dust from the boundary layer. However, the present analysis does not allow a robust assessment of the wet deposition parameterization because the model evaluation point is located approximately 40 km from the observation site and precipitation was spatially heterogeneous. Consequently, differences between simulated and observed dust concentrations may partly reflect spatial displacement of precipitation rather than deficiencies in the wet removal scheme itself. Wet deposition should therefore be regarded as an important physical process that requires further investigation using more closely collocated precipitation observations.

Overall, the results indicate that further improvements in the simulation of long-range Saharan dust transport should focus on two largely independent aspects. Meteorological initialization together with convection-permitting resolution substantially improves the timing, vertical distribution, and surface concentrations of transported dust. In contrast, the persistent coarse-particle deficit and associated optical discrepancies remain largely insensitive to these improvements and instead reflect limitations in the current aerosol representation. Future model development should therefore focus on improving the representation of the emitted coarse-particle size distribution and size-dependent sedimentation and deposition processes and on extending the aerosol representation to include ageing and mixing processes that modify aerosol optical properties.

5 Conclusions

This study combined vertically resolved lidar observations, sun-photometer and in situ measurements, satellite products, backward trajectories, and ICON-ART simulations to investigate four contrasting Saharan dust events over southwestern Germany. The selected cases covered prolonged clear-sky transport, dust–cloud interactions, and an intense dust outbreak, providing a range of observational constraints on

Saharan dust transport, vertical structure, optical properties, and boundary-layer entrainment.

ICON-ART reproduced the regional transport pathways and arrival of the Saharan air layers well, demonstrating that the model captures the synoptic-scale processes controlling long-range dust transport towards Western Europe. Separating the lidar-derived backscatter into dust and non-dust components enabled a consistent comparison with the modelled dust field and avoided attributing the contribution of other aerosols to model error. This separation provides an important constraint for evaluating dust transport in mixed aerosol layers.

The sensitivity experiments for the February 2021 event show that meteorological forcing and horizontal resolution play complementary roles, with daily reinitialization producing the more substantial improvement. Daily reinitialization of the global simulation updated the lateral boundary conditions and improved the timing and persistence of dust within the boundary layer. Comparisons with radiosonde observations showed that daily reinitialization generally reduced temperature and wind-profile errors, whereas increasing horizontal resolution alone did not consistently improve meteorological agreement. Within RI-EXP-1d, the convection-permitting simulations showed additional, localized improvements in the vertical dust distribution through reduced overestimation of backscatter in elevated dust layers. These benefits were comparatively modest and did not extend consistently to all diagnostics, including column-integrated AOD. Thus, higher resolution alone does not necessarily translate into a better dust forecast, and the resolution-dependent benefits identified here remain specific to the February 2021 case.

In contrast, persistent biases in particle size and associated optical properties were largely insensitive to meteorological initialization and grid spacing. ICON-ART shifted the transported dust towards smaller particle sizes, overestimating particles between approximately 0.5 and 2 µm while underestimating particles larger than 2 µm. The results therefore suggest that transport-related and aerosol-process errors are partly separable: improved meteorological forcing can improve plume timing and vertical distribution, with finer resolution providing additional benefits in selected profiles, whereas the persistent coarse-particle deficit points to possible limitations in the representation of coarse-dust emissions and size-dependent removal processes.

Overall, the combination of vertically resolved and size-resolved observations provides a means of distinguishing dynamical from aerosol-process limitations in long-range dust simulations. Future model development should therefore prioritize the joint improvement of lateral meteorological forcing and coarse-dust process representation. This will require targeted evaluation of coarse-particle emissions and removal processes together with more closely collocated observations of aerosol size, composition, clouds, and precipitation.

Code availability. The code used to analyse the lidar data is property of Raymetrics Inc, but we have shown that it generates the same results as the code single calculus chain (SCC) provided by EARLIENT https://earlinet.eu/our-knowledge/access-to-software/, last access: 5 November 2026). The ICON-ART model is open-source and accessible through https://doi.org/10.5281/zenodo.20762965 (Max Planck Institute for Meteorology et al., 2026).

Data availability. The lidar raw data and in situ data are available via the open access data repository KIT open (https://doi.org/10.35097/6hm7pus0e79ztvub, Zhang et al., 2026). Sun photometer data are available from the AErosol RObotic NETwork (Aeronet) data center at https://aeronet.gsfc.nasa.gov/, last access: 5 November 2026). ICON-ART model simulation results are available upon request from the data originator (DWD; datenservice@dwd.de and KIT; gholamali.hoshyaripour@kit.edu).

Supplement. The supplement related to this article is available online at https://doi.org/10.5194/acp-26-16545-2026-supplement.

Author contributions. FW, HS, and HZ performed the measurements. GAH, HV, JF conducted the model simulations and post processing of the outputs. PS performed the high-resolution simulations and post-processing of model and satellite datasets. HZ and FW analysed the remote sensing data. HZ did write the manuscript with support from FW and HS as well as contributions from all co-authors.

Competing interests. At least one of the (co-)authors is a member of the editorial board of *Atmospheric Chemistry and Physics*. The peer-review process was guided by an independent editor, and the authors also have no other competing interests to declare.

Disclaimer. Publisher's note: Copernicus Publications remains neutral with regard to jurisdictional claims made in the text, published maps, institutional affiliations, or any other geographical representation in this paper. The authors bear the ultimate responsibility for providing appropriate place names. Views expressed in the text are those of the authors and do not necessarily reflect the views of the publisher.

Acknowledgements. Support by the staff of the Institute of Meteorology and Climate Research, and support by the project Modular Observation Solutions for Earth Systems (MOSES) of the Helmholtz Association (HGF). This work contributes to and is partly funded by the GLObal-to-Regional ICON Digital Twin (GLORI) project.

Financial support. The article processing charges for this open-access publication were covered by the Karlsruhe Institute of Technology (KIT).

Review statement. This paper was edited by Fangqun Yu and reviewed by Yan Yu and one anonymous referee.

References

Adebiyi, A. A. and Kok, J. F.: Climate models miss most of the coarse dust in the atmosphere, Science Advances, 6, eaaz9507, https://doi.org/10.1126/sciadv.aaz9507, 2020.

Ansmann, A., BÃ¶senberg, J., Chaikovsky, A., Comerón, A., Eckhardt, S., Eixmann, R., Freudenthaler, V., Ginoux, P., Komguem, L., Linné, H., MÃ¡rquez, M. Ã. L., Matthias, V., Mattis, I., Mitev, V., Müller, D., Music, S., Nickovic, S., Pelon, J., Sauvage, L., Sobolewsky, P., Srivastava, M. K., Stohl, A., Torres, O., Vaughan, G., Wandinger, U., and Wiegner, M.: Long-range transport of Saharan dust to northern Europe: The 11–16 October 2001 outbreak observed with EARLINET, J. Geophys. Res.-Atmos., 108, https://doi.org/10.1029/2003JD003757, 2003.

Avdikos, G.: Powerful Raman Lidar systems for atmospheric analysis and high-energy physics experiments, EPJ Web Conf., 89, 04003, https://doi.org/10.1051/epjconf/20158904003, 2015.

Barnaba, F. and Gobbi, G. P.: Aerosol seasonal variability over the Mediterranean region and relative impact of maritime, continental and Saharan dust particles over the basin from MODIS data in the year 2001, Atmos. Chem. Phys., 4, 2367–2391, https://doi.org/10.5194/acp-4-2367-2004, 2004.

Benincasa, F.: Forecast comparison – WMO SDS-WAS, https://dust.aemet.es/products/daily-dust-products (last access: 5 November 2026)., 2023.

Cao, C., Zheng, S., and Singh, R. P.: Characteristics of aerosol optical properties and meteorological parameters during three major dust events (2005–2010) over Beijing, China, Atmos. Res., 150, 129–142, https://doi.org/10.1016/j.atmosres.2014.07.022, 2014.

Chapman, E. G., Gustafson Jr., W. I., Easter, R. C., Barnard, J. C., Ghan, S. J., Pekour, M. S., and Fast, J. D.: Coupling aerosol-cloud-radiative processes in the WRF-Chem model: Investigating the radiative impact of elevated point sources, Atmos. Chem. Phys., 9, 945–964, https://doi.org/10.5194/acp-9-945-2009, 2009.

Chouza, F., Reitebuch, O., Benedetti, A., and Weinzierl, B.: Saharan dust long-range transport across the Atlantic studied by an airborne Doppler wind lidar and the MACC model, Atmos. Chem. Phys., 16, 11581–11600, https://doi.org/10.5194/acp-16-11581-2016, 2016.

Conceição, R., Silva, H. G., Mirão, J., Gostein, M., Fialho, L., Narvarte, L., and Collares-Pereira, M.: Saharan dust transport to Europe and its impact on photovoltaic performance: A case study of soiling in Portugal, Sol. Energy, 160, 94–102, https://doi.org/10.1016/j.solener.2017.11.059, 2018.

Diop, D., Niang, D. N., Drame, M. S., and Ba, A.: Dust Source, Vertical Profile and Climate Impact by RegCM3 Regional Climate Model over West Africa during 2006, Atmospheric and Climate Sciences, 10, 206–219, https://doi.org/10.4236/acs.2020.102011, 2020.

Dubovik, O. and King, M. D.: A flexible inversion algorithm for retrieval of aerosol optical properties from Sun and sky radiance measurements, J. Geophys. Res.-Atmos., 105, 20673–20696, https://doi.org/10.1029/2000JD900282, 2000.

Freudenthaler, V.: About the effects of polarising optics on lidar signals and the Δ90 calibration, Atmos. Meas. Tech., 9, 4181–4255, https://doi.org/10.5194/amt-9-4181-2016, 2016.

Freudenthaler, V., Esselborn, M., Wiegner, M., Heese, B., Tesche, M., Ansmann, A., Müller, D., Althausen, D., Wirth, M., Fix, A., Ehret, G., Knippertz, P., Toledano, C., Gasteiger, J., Garhammer, M., and Seefeldner, M.: Depolarization ratio profiling at several wavelengths in pure Saharan dust during SAMUM 2006, Tellus B, 61, 165–179, https://doi.org/10.1111/j.1600-0889.2008.00396.x, 2009.

Gasteiger, J., Wiegner, M., Groß, S., Freudenthaler, V., Toledano, C., Tesche, M., and Kandler, K.: Modelling lidar-relevant optical properties of complex mineral dust aerosols, Tellus B, 63, 725–741, https://doi.org/10.1111/j.1600-0889.2011.00559.x, 2011.

Giles, D. M., Sinyuk, A., Sorokin, M. G., Schafer, J. S., Smirnov, A., Slutsker, I., Eck, T. F., Holben, B. N., Lewis, J. R., Campbell, J. R., Welton, E. J., Korkin, S. V., and Lyapustin, A. I.: Advancements in the Aerosol Robotic Network (AERONET) Version 3 database – automated near-real-time quality control algorithm with improved cloud screening for Sun photometer aerosol optical depth (AOD) measurements, Atmos. Meas. Tech., 12, 169–209, https://doi.org/10.5194/amt-12-169-2019, 2019.

Groß, S., Tesche, M., Freudenthaler, V., Toledano, C., Wiegner, M., Ansmann, A., Althausen, D., and Seefeldner, M.: Characterization of Saharan dust, marine aerosols and mixtures of biomass-burning aerosols and dust by means of multi-wavelength depolarization and Raman lidar measurements during SAMUM 2, Tellus B, 63, 706–724, https://doi.org/10.1111/j.1600-0889.2011.00556.x, 2011.

Guerzoni, S. and Chester, R. (Eds.): The Impact of Desert Dust Across the Mediterranean, vol. 11, Environmental Science and Technology Library, Springer Netherlands, Dordrecht, ISBN 978-90-481-4764-9 978-94-017-3354-0, https://doi.org/10.1007/978-94-017-3354-0, 1996.

Haarig, M., Ansmann, A., Gasteiger, J., Kandler, K., Althausen, D., Baars, H., Radenz, M., and Farrell, D. A.: Dry versus wet marine particle optical properties: RH dependence of depolarization ratio, backscatter, and extinction from multiwavelength lidar measurements during SALTRACE, Atmos. Chem. Phys., 17, 14199–14217, https://doi.org/10.5194/acp-17-14199-2017, 2017.

Haarig, M., Ansmann, A., Engelmann, R., Baars, H., Toledano, C., Torres, B., Althausen, D., Radenz, M., and Wandinger, U.: First triple-wavelength lidar observations of depolarization and extinction-to-backscatter ratios of Saharan dust, Atmos. Chem. Phys., 22, 355–369, https://doi.org/10.5194/acp-22-355-2022, 2022.

Hermes, K., Quinting, J., Grams, C. M., Hoose, C., and Hoshyaripour, G. A.: Impact of Saharan dust outbreaks on short-range weather forecast errors in Europe, Q. J. Roy. Meteor. Soc., 150, 1704–1723, https://doi.org/10.1002/qj.4666, 2024.

Holben, B. N., Eck, T. F., Slutsker, I., Tanré, D., Buis, J. P., Setzer, A., Vermote, E., Reagan, J. A., Kaufman, Y. J., Nakajima, T., Lavenu, F., Jankowiak, I., and Smirnov, A.: AERONET – A federated instrument network and data archive for aerosol characterization, Remote Sens. Environ., 66, 1–16, https://doi.org/10.1016/S0034-4257(98)00031-5, 1998.

Hoshyaripour, G. A., Bachmann, V., Förstner, J., Steiner, A., Vogel, H., Wagner, F., Walter, C., and Vogel, B.: Effects of Particle Nonsphericity on Dust Optical Properties

in a Forecast System: Implications for Model-Observation Comparison, J. Geophys. Res.-Atmos., 124, 7164–7178, https://doi.org/10.1029/2018JD030228, 2019.

Hoshyaripour, G. A., Baer, A., Bierbauer, S., Bruckert, J., Brunner, D., Förstner, J., Hamzehloo, A., Hanft, V., Keller, C., Klose, M., Kumar, P., Ludwig, P., Metzner, E., Muth, L., Pauling, A., Porz, N., Ramezani Ziarani, M., Reddmann, T., Reißig, L., Ruhnke, R., Satitkovitchai, K., Seifert, A., Sinnhuber, M., Steiner, M., Versick, S., Vogel, H., Weimer, M., Werchner, S., and Hoose, C.: The atmospheric composition component of the ICON modeling framework: ICON-ART version 2025.10, Geosci. Model Dev., 19, 1645–1681, https://doi.org/10.5194/gmd-19-1645-2026, 2026.

Jiang, F., Saathoff, H., Ezenobi, U., Song, J., Zhang, H., Gao, L., and Leisner, T.: Measurement report: Brown carbon aerosol in rural Germany – sources, chemistry, and diurnal variations, Atmos. Chem. Phys., 25, 1917–1930, https://doi.org/10.5194/acp-25-1917-2025, 2025.

Jöckel, P., Tost, H., Pozzer, A., Brühl, C., Buchholz, J., Ganzeveld, L., Hoor, P., Kerkweg, A., Lawrence, M. G., Sander, R., Steil, B., Stiller, G., Tanarhte, M., Taraborrelli, D., van Aardenne, J., and Lelieveld, J.: The atmospheric chemistry general circulation model ECHAM5/MESSy1: consistent simulation of ozone from the surface to the mesosphere, Atmos. Chem. Phys., 6, 5067–5104, https://doi.org/10.5194/acp-6-5067-2006, 2006.

Jöckel, P., Kerkweg, A., Pozzer, A., Sander, R., Tost, H., Riede, H., Baumgaertner, A., Gromov, S., and Kern, B.: Development cycle 2 of the Modular Earth Submodel System (MESSy2), Geosci. Model Dev., 3, 717–752, https://doi.org/10.5194/gmd-3-717-2010, 2010.

Kandler, K., Benker, N., Bundke, U., Cuevas, E., Ebert, M., Knippertz, P., Rodríguez, S., Schütz, L., and Weinbruch, S.: Chemical composition and complex refractive index of Saharan Mineral Dust at Izaña, Tenerife (Spain) derived by electron microscopy, Atmos. Environ., 41, 8058–8074, https://doi.org/10.1016/j.atmosenv.2007.06.047, 2007.

Kanngießer, F. and Fiedler, S.: Intercomparison case study of data-driven reconstructions of a cloud-obscured Saharan dust plume in Europe, Sci. Rep., 16, 17165, https://doi.org/10.1038/s41598-026-55422-y, 2026.

Kim, D., Chin, M., Yu, H., Eck, T. F., Sinyuk, A., Smirnov, A., and Holben, B. N.: Dust optical properties over North Africa and Arabian Peninsula derived from the AERONET dataset, Atmos. Chem. Phys., 11, 10733–10741, https://doi.org/10.5194/acp-11-10733-2011, 2011.

Kunz, A., Pan, L. L., Konopka, P., Kinnison, D. E., and Tilmes, S.: Chemical and dynamical discontinuity at the extratropical tropopause based on START08 and WACCM analyses, J. Geophys. Res.-Atmos., 116, https://doi.org/10.1029/2011JD016686, 2011.

Kunz, M., Abbas, S. S., Bauckholt, M., Böhmländer, A., Feuerle, T., Gasch, P., Glaser, C., Groß, J., Hajnsek, I., Handwerker, J., Hase, F., Khordakova, D., Knippertz, P., Kohler, M., Lange, D., Latt, M., Laube, J., Martin, L., Mauder, M., Möhler, O., Mohr, S., Reitter, R. W., Rettenmeier, A., Rolf, C., Saathoff, H., Schrön, M., Schütze, C., Spahr, S., Späth, F., Vogel, F., Völksch, I., Weber, U., Wieser, A., Wilhelm, J., Zhang, H., and Dietrich, P.: Swabian MOSES 2021: An interdisciplinary field campaign for investigating convective storms and their event chains, Front. Earth Sci., 10, https://doi.org/10.3389/feart.2022.999593, 2022.

Liu, Z., Omar, A., Vaughan, M., Hair, J., Kittaka, C., Hu, Y., Powell, K., Trepte, C., Winker, D., Hostetler, C., Ferrare, R., and Pierce, R.: CALIPSO lidar observations of the optical properties of Saharan dust: A case study of long-range transport, J. Geophys. Res.-Atmos., 113, https://doi.org/10.1029/2007JD008878, 2008.

Mallet, M., Tulet, P., Serça, D., Solmon, F., Dubovik, O., Pelon, J., Pont, V., and Thouron, O.: Impact of dust aerosols on the radiative budget, surface heat fluxes, heating rate profiles and convective activity over West Africa during March 2006, Atmos. Chem. Phys., 9, 7143–7160, https://doi.org/10.5194/acp-9-7143-2009, 2009.

Max Planck Institute for Meteorology, German Meteorological Service, German Climate Computing Centre, Karlsruhe Institute of Technology, and Center for Climate Systems Modeling: ICON 2026.04 Release (Version 2026.04), Zenodo [code], https://doi.org/10.5281/zenodo.20762965, 2026.

Merdji, A. B., Lu, C., Xu, X., and Mhawish, A.: Long-term three-dimensional distribution and transport of Saharan dust: Observation from CALIPSO, MODIS, and reanalysis data, Atmos. Res., 286, 106658, https://doi.org/10.1016/j.atmosres.2023.106658, 2023.

Middleton, N. J. and Goudie, A. S.: Saharan dust: sources and trajectories, T. I. Brit. Geogr., 26, 165–181, https://doi.org/10.1111/1475-5661.00013, 2001.

Misra, A., Tripathi, S. N., Kaul, D. S., and Welton, E. J.: Study of MPLNET-Derived Aerosol Climatology over Kanpur, India, and Validation of CALIPSO Level 2 Version 3 Backscatter and Extinction Products, J. Atmos. Ocean. Tech., 29, 1285–1294, https://doi.org/10.1175/JTECH-D-11-00162.1, 2012.

Molinaroli, E., Guerzoni, S., and Rampazzo, G.: Contribution of Saharan dust to the Central Mediterranean Basin, in: Processes Controlling the Composition of Clastic Sediments, edited by: Johnsson, M. J. and Basu, A., vol. 284, Geological Society of America, ISBN 978-0-8137-2284-9, https://doi.org/10.1130/SPE284-p303, 1993.

Mona, L., Papagiannopoulos, N., Basart, S., Baldasano, J., Binietoglou, I., Cornacchia, C., and Pappalardo, G.: EARLINET dust observations vs. BSC-DREAM8b modeled profiles: 12-year-long systematic comparison at Potenza, Italy, Atmos. Chem. Phys., 14, 8781–8793, https://doi.org/10.5194/acp-14-8781-2014, 2014.

Müller, D., Weinzierl, B., Petzold, A., Kandler, K., Ansmann, A., MÃ¼ller, T., Tesche, M., Freudenthaler, V., Esselborn, M., Heese, B., Althausen, D., Schladitz, A., Otto, S., and Knippertz, P.: Mineral dust observed with AERONET Sun photometer, Raman lidar, and in situ instruments during SAMUM 2006: Shape-independent particle properties, J. Geophys. Res.-Atmos., 115, https://doi.org/10.1029/2009JD012520, 2010.

Müller, D., Lee, K.-H., Gasteiger, J., Tesche, M., Weinzierl, B., Kandler, K., Müller, T., Toledano, C., Otto, S., Althausen, D., and Ansmann, A.: Comparison of optical and microphysical properties of pure Saharan mineral dust observed with AERONET Sun photometer, Raman lidar, and in situ instruments during SAMUM 2006, J. Geophys. Res.-Atmos., 117, https://doi.org/10.1029/2011JD016825, 2012.

Pozzoli, L., Bey, I., Rast, S., Schultz, M. G., Stier, P., and Feichter, J.: Trace gas and aerosol interactions in the

fully coupled model of aerosol-chemistry-climate ECHAM5-HAMMOZ: 1. Model description and insights from the spring 2001 TRACE-P experiment, J. Geophys. Res.-Atmos., 113, https://doi.org/10.1029/2007JD009007, 2008a.

Pozzoli, L., Bey, I., Rast, S., Schultz, M. G., Stier, P., and Feichter, J.: Trace gas and aerosol interactions in the fully coupled model of aerosol-chemistry-climate ECHAM5-HAMMOZ: 2. Impact of heterogeneous chemistry on the global aerosol distributions, J. Geophys. Res.-Atmos., 113, https://doi.org/10.1029/2007JD009008, 2008b.

Ratcliffe, N. G., Ryder, C. L., Bellouin, N., Jones, A., Johnson, B., Woodward, S., Wieland, L.-M., Gasteiger, J., and Weinzierl, B.: New processes to counteract sedimentation of coarse dust particles are required for climate models to agree with aircraft observations, EGUsphere [preprint], https://doi.org/10.5194/egusphere-2025-5143, 2025.

Rieger, D., Bangert, M., Bischoff-Gauss, I., Förstner, J., Lundgren, K., Reinert, D., Schröter, J., Vogel, H., Zängl, G., Ruhnke, R., and Vogel, B.: ICON–ART 1.0 – a new online-coupled model system from the global to regional scale, Geosci. Model Dev., 8, 1659–1676, https://doi.org/10.5194/gmd-8-1659-2015, 2015.

Rieger, D., Steiner, A., Bachmann, V., Gasch, P., Förstner, J., Deetz, K., Vogel, B., and Vogel, H.: Impact of the 4 April 2014 Saharan dust outbreak on the photovoltaic power generation in Germany, Atmos. Chem. Phys., 17, 13391–13415, https://doi.org/10.5194/acp-17-13391-2017, 2017a.

Rieger, D., Steiner, A., Bachmann, V., Gasch, P., Förstner, J., Deetz, K., Vogel, B., and Vogel, H.: Impact of the 4 April 2014 Saharan dust outbreak on the photovoltaic power generation in Germany, Atmos. Chem. Phys., 17, 13391–13415, https://doi.org/10.5194/acp-17-13391-2017, 2017b.

Roeckner, E., Brokopf, R., Esch, M., Giorgetta, M., Hagemann, S., Kornblueh, L., Manzini, E., Schlese, U., and Schulzweida, U.: Sensitivity of Simulated Climate to Horizontal and Vertical Resolution in the ECHAM5 Atmosphere Model, J. Climate, 19, 3771–3791, https://doi.org/10.1175/JCLI3824.1, 2006.

Rostási, Ã., Topa, B. A., Gresina, F., Weiszburg, T. G., Gelencsér, A., and Varga, G.: Saharan Dust Deposition in Central Europe in 2016 – A Representative Year of the Increased North African Dust Removal Over the Last Decade, Front. Earth Sci., 10, https://doi.org/10.3389/feart.2022.869902, 2022.

Saidou Chaibou, A. A., Ma, X., and Sha, T.: Dust radiative forcing and its impact on surface energy budget over West Africa, Sci. Rep., 10, 12236, https://doi.org/10.1038/s41598-020-69223-4, 2020.

Schuster, G. L., Vaughan, M., MacDonnell, D., Su, W., Winker, D., Dubovik, O., Lapyonok, T., and Trepte, C.: Comparison of CALIPSO aerosol optical depth retrievals to AERONET measurements, and a climatology for the lidar ratio of dust, Atmos. Chem. Phys., 12, 7431–7452, https://doi.org/10.5194/acp-12-7431-2012, 2012.

Seifert, A., Bachmann, V., Filipitsch, F., Förstner, J., Grams, C. M., Hoshyaripour, G. A., Quinting, J., Rohde, A., Vogel, H., Wagner, A., and Vogel, B.: Aerosol–cloud–radiation interaction during Saharan dust episodes: the dusty cirrus puzzle, Atmos. Chem. Phys., 23, 6409–6430, https://doi.org/10.5194/acp-23-6409-2023, 2023.

Sinyuk, A., Holben, B. N., Eck, T. F., Giles, D. M., Slutsker, I., Korkin, S., Schafer, J. S., Smirnov, A., Sorokin, M., and Lyapustin, A.: The AERONET Version 3 aerosol retrieval algorithm, associated uncertainties and comparisons to Version 2, Atmos. Meas. Tech., 13, 3375–3411, https://doi.org/10.5194/amt-13-3375-2020, 2020.

Smith, K., Garcia, R., Marsh, D., and Richter, H.: WACCM simulations of the mean circulation and trace species transport in the winter mesosphere, J. Geophys. Res.-Atmos., https://doi.org/10.1029/2011JD016083, 2011.

Song, Q., Zhang, Z., Yu, H., Kok, J. F., Di Biagio, C., Albani, S., Zheng, J., and Ding, J.: Size-resolved dust direct radiative effect efficiency derived from satellite observations, Atmos. Chem. Phys., 22, 13115–13135, https://doi.org/10.5194/acp-22-13115-2022, 2022.

Sugimoto, N., Nishizawa, T., Shimizu, A., and Jin, Y.: The Asian Dust and Aerosol Lidar Observation Network (AD-Net), in: Light, Energy and the Environment (2016), paper EW2A.1, EW2A.1, Optica Publishing Group, https://doi.org/10.1364/EE.2016.EW2A.1, 2016.

Tanaka, T. Y., Kurosaki, Y., Chiba, M., Matsumura, T., Nagai, T., Yamazaki, A., Uchiyama, A., Tsunematsu, N., and Kai, K.: Possible transcontinental dust transport from North Africa and the Middle East to East Asia, Atmos. Environ., 39, 3901–3909, https://doi.org/10.1016/j.atmosenv.2005.03.034, 2005.

Tesche, M., Ansmann, A., Müller, D., Althausen, D., Engelmann, R., Freudenthaler, V., and Groß, S.: Vertically resolved separation of dust and smoke over Cape Verde using multiwavelength Raman and polarization lidars during Saharan Mineral Dust Experiment 2008, J. Geophys. Res.-Atmos., 114, https://doi.org/10.1029/2009JD011862, 2009a.

Tesche, M., Ansmann, A., Müller, D., Althausen, D., Engelmann, R., Freudenthaler, V., and Groß, S.: Vertically resolved separation of dust and smoke over Cape Verde using multiwavelength Raman and polarization lidars during Saharan Mineral Dust Experiment 2008, J. Geophys. Res.-Atmos., 114, https://doi.org/10.1029/2009JD011862, 2009b.

Varga, G.: Changing nature of Saharan dust deposition in the Carpathian Basin (Central Europe): 40 years of identified North African dust events (1979–2018), Environ. Int., 139, 105712, https://doi.org/10.1016/j.envint.2020.105712, 2020.

Vermeulen, A., Devaux, C., and Herman, M.: Retrieval of the scattering and microphysical properties of aerosols from ground-based optical measurements including polarization. I. Method, Appl. Opt., 39, 6207–6220, https://doi.org/10.1364/AO.39.006207, 2000.

Vogel, B., Hoose, C., Vogel, H., and Kottmeier, C.: A model of dust transport applied to the Dead Sea Area, Meteorol. Z., 611–624, https://doi.org/10.1127/0941-2948/2006/0168, 2006.

Vogel, H., Förstner, J., Vogel, B., Hanisch, T., Mühr, B., Schättler, U., and Schad, T.: Time-lagged ensemble simulations of the dispersion of the Eyjafjallajökull plume over Europe with COSMO-ART, Atmos. Chem. Phys., 14, 7837–7845, https://doi.org/10.5194/acp-14-7837-2014, 2014.

Weimer, M., Schröter, J., Eckstein, J., Deetz, K., Neumaier, M., Fischbeck, G., Hu, L., Millet, D. B., Rieger, D., Vogel, H., Vogel, B., Reddmann, T., Kirner, O., Ruhnke, R., and Braesicke, P.: An emission module for ICON-ART 2.0: implementation and simulations of acetone, Geosci. Model Dev., 10, 2471–2494, https://doi.org/10.5194/gmd-10-2471-2017, 2017.

Wu, M., Liu, X., Yu, H., Wang, H., Shi, Y., Yang, K., Darmenov, A., Wu, C., Wang, Z., Luo, T., Feng, Y., and Ke, Z.: Understanding processes that control dust spatial distributions with global climate models and satellite observations, Atmos. Chem. Phys., 20, 13835–13855, https://doi.org/10.5194/acp-20-13835-2020, 2020.

Zhang, H., Wagner, F., Saathoff, H., Vogel, H., Hoshyaripour, G., Bachmann, V., Förstner, J., and Leisner, T.: Comparison of Scanning LiDAR with Other Remote Sensing Measurements and Transport Model Predictions for a Saharan Dust Case, Remote Sensing, 14, 1693, https://doi.org/10.3390/rs14071693, 2022.

Zhang, H., Hoshyaripour, G. A., Vogel, H., Wagner, F., Leisner, T., Förstner, J., Shrestha, P., and Saathoff, H.: Dataset: Saharan dust transport and boundary layer entrainment over Western Europe: multi-instrument observations and convection-permitting model evaluation, Karlsruhe Institute of Technology [data set], https://doi.org/10.35097/6hm7pus0e79ztvub, 2026.

Zo, I.-S. and Shin, S.-K.: A Short Note on the Potential of Utilization of Spectral AERONET-Derived Depolarization Ratios for Aerosol Classification, Atmosphere, 10, https://doi.org/10.3390/atmos10030143, 2019.

Zängl, G., Reinert, D., Rípodas, P., and Baldauf, M.: The ICON (ICOsahedral Non-hydrostatic) modelling framework of DWD and MPI-M: Description of the non-hydrostatic dynamical core, Q. J. Roy. Meteor. Soc., 141, 563–579, https://doi.org/10.1002/qj.2378, 2015.